UNIVERSITY OF OKLAHOMA

GRADUATE COLLEGE

ELUCIDATING QUATERNARY HIGH-FREQUENCY DEPOSITIONAL SEQUENCES AND INCISED VALLEY EVOLUTION USING HIGH-RESOLUTION 3D SEISMIC DATA: GULF OF MEXICO, USA

A THESIS

SUBMITTED TO THE GRADUATE FACULTY

in partial fulfillment of the requirements for the

Degree of

MASTER OF SCIENCE

By

Jacob Maag

Norman, Oklahoma

2024

Downloaded from SHAREOK. Persistent Handle URL: https://hdl.handle.net/11244/340244

ELUCIDATING QUATERNARY HIGH-FREQUENCY DEPOSITIONAL SEQUENCES AND INCISED VALLEY EVOLUTION USING HIGH-RESOLUTION 3D SEISMIC DATA: GULF OF MEXICO, USA

A THESIS APPROVED FOR THE

SCHOOL OF GEOSCIENCES

BY THE COMMITTEE CONSISTING OF

Dr. Heather Bedle, Chair

Dr. Matthew Pranter

Dr. Sarah George

© Copyright by JACOB MAAG 2024

All Rights Reserved

ACKNOWLEDGEMENTS

First, I want to thank God for giving me the strength to face the adversity encountered throughout my academic career. Next, I want to thank my mother, father, and grandparents for always encouraging me to pursue my dreams and for instilling a strong work ethic in me at a young age; without their guidance, support, and discipline, I would not be where I am today. I also want to thank my better half, Aliyah, for her unwavering support and encouragement throughout my educational journey.

Importantly, I want to thank my advisor and committee chair, Dr. Heather Bedle, for taking me in upon the unexpected passing of my previous advisor, Dr. John Pigott, and allowing me to continue my graduate studies at the University of Oklahoma. Words cannot describe how immensely grateful I am for this selfless act. I also want to thank the sponsors of Attribute-Assisted Seismic Processing and Interpretation (AASPI) for providing me with funding for the final year of my master's degree. Additionally, I want to thank all of my committee members—Dr. Heather Bedle, Dr. Matthew Pranter, and Dr. Sarah George—for their assistance throughout this project. Lastly, I want to thank all of my peers and colleagues as their advice and input was instrumental to the successful completion of my master's degree.

TABLE OF CONTENTS

Acknowledgements ..... **iv**
Abstract ..... **xiii**
Introduction **1**
Geological Background **2**
Regional Basin Evolution 2
Inner Shelf Quaternary Geology and Sea Level Changes 3
Brazos and Trinity River Systems 5
Study Area Geology 6
Data **7**
Limitations of Conventional 3D Seismic Data 7
HR3D Seismic Survey 9
HR3D Seismic Resolution 10
Methods **12**
Data Loading and Conditioning 12
Unconformity Identification and Mapping 13
Unconformity Time-to-Depth Conversions 14
Seismic Attributes 15
Spectrally Balanced Amplitude 15
Sweetness 15
Sobel Filter 16
Most-Positive (K_1) Curvature and Most-Negative (K_2) Curvature 16
Valley Shape 17
Sequence Stratigraphy 17
Valley Evolution 18
Machine Learning 18
Principal Component Analysis (PCA) 19
Results **19**
Data Conditioning and Spectral Balancing 19
Unconformity Time-Structure Maps 21
Seismic Attributes 23
Spectrally Balanced Amplitude 24
Sweetness 25

Sobel Filter 26
Most-Positive (K_1) Curvature and Most-Negative (K_2) Curvature 27
Valley Shape 29
Machine Learning: Principal Component Analysis (PCA) 30
Discussion 32
Overview of HR3D Fluvial Features 32
Interaction Between Low Gradient Shelf and Frequent Sea Level Changes 33
Importance of Unconformities and Incised Valleys in Sequence Stratigraphy 33
Correlating the Upper Unconformity to a Eustatic Lowstand Event 34
Correlating the Middle Unconformity to a Eustatic Lowstand Event 36
Correlating the Lower Unconformity to a Eustatic Lowstand Event 38
HR3D Sequence Stratigraphy 38
Orders of Sea Level Cyclicity and Hierarchy 41
Fifth-Order Implications for Hydrocarbon Reservoirs 43
Valley Evolution 44
Valley Evolution in Response to Transgression 45
Inferring Lithology from Principal Component Analysis (PCA) Results 47
Conclusions 49
References 51
Appendices 57
Appendix A. Frequency distribution through the interval of interest—0 to 200 milliseconds..57
Appendix B. Peak frequency extracted along each unconformity. 57
Appendix C. Peak magnitude extracted along each unconformity. 58
Appendix D. Spectrally balanced amplitude extracted along the maximum flooding surfaces (MFS) of each depositional sequence. 58
Appendix E. Sweetness extracted along the maximum flooding surfaces (MFS) of each depositional sequence. 59

LIST OF FIGURES

Figure 1. Modified from Johnson and Watt (2012). Late Quaternary eustatic sea level curve spanning from present to 400,000 years. In this span of time, five highstand events (blue asterisks) and four lowstand events (orange asterisks) occurred……..….4

Figure 2. Seismic inline 230 showing the major geologic elements as also identified by Meckel and Mulcahy (2016) within the HR3D volume. The survey encompasses several common GoM features—salt (pink), normal faults (black), unconformities (orange), sea floor (red) etc……...….7

Figure 3. Comparison of high-resolution 3D (HR3D) seismic (peak frequency = 130 Hz) to conventional 3D (C3D) seismic (peak frequency = 40 Hz) from the San Luis Pass area. To the right, the sea level curves are vertically scaled to the average thickness—in this case, time—of their stated depositional sequences (first, second, third, fourth, and fifth). Due to shallow water depths and large bin sizes, important data is muted throughout the shallowest 475 ms of the C3D volume (i.e., the interval of interest). Additionally, while fourth and fifth order sequences may appear within the C3D volume as single peaks or troughs, the resolution is not sufficient for a seismic stratigraphic analysis of the sequences. In contrast, no important data is muted within the HR3D volume, and the vertical resolution permits the analysis of fourth and fifth order depositional sequences…….8

Figure 4. Geographic location of the study area located approximately16 km south of San Luis Pass, Texas indicated by the red polygon. The HR3D seismic survey covers a small area of 29 km2…….……..……..10

Figure 5. The implemented workflow for this study……..…….12

Figure 6. Interpreted unconformities along seismic inline 195. The unconformities were assigned names of Lower Unconformity (LUC), Middle Unconformity (MUC), and Upper Unconformity (UUC). Each unconformity is characterized by the lateral truncation of seismic reflectors as indicated by red arrows……..……13

Figure 7. Comparison of the original vs. filtered data using the Sobel filter attribute along a time slice of 0.05 seconds. Green arrows indicate areas where the filtered volume demonstrates reduced acquisition footprint, and blue arrows indicate areas where the filtered volume demonstrates enhanced geologic features…….…..….20

Figure 8. Comparison of the original vs. spectrally balanced amplitude along a time slice of 0.11 seconds. The spectrally balanced volume exhibits a further enhanced signal-to-noise ratio and improved resolution. The green arrows indicate channel margins and architectural elements which are more well-defined along the spectrally balanced time slice……..…….21

Figure 9. Corendered time-structure and amplitude along each unconformity. The LUC contains a south-trending channel accompanied by numerous dendritic tributaries. The MUC contains a large meandering south-trending channel accompanied by a complex network of dendritic tributaries and crevasse splays. The UUC consists of a main channel accompanied by numerous dendritic tributaries. The blue arrows indicate the main channels, and the green arrows indicate dendritic tributaries and crevasse splays. The orange arrows indicate the salt diapir. The red arrow indicates the Salina Fault, and the yellow arrows indicate the visible Incrementum Faults……..23

Figure 10. Spectrally balanced amplitude extracted along each unconformity. The attribute permits the visualization of subtle channels and amplitude anomalies throughout the volume. The green arrows indicate subtle channels which were not visible in the original amplitude volume,

and the red arrows indicate negative amplitude anomalies. The northeast-southwest trending acquisition footprint becomes more prominent with decreasing depth……...25

Figure 11. Sweetness attribute extracted along each unconformity. The attribute permits further visualization of subtle channels and highlights sands (high values) and shales (low values). The green arrows indicate subtle channels which were revealed by sweetness, and the red arrows indicate abnormally high sweetness anomalies. The northeast-southwest trending acquisition footprint becomes more prominent with decreasing depth…….26

Figure 12. Sobel filter attribute extracted along each unconformity. The attribute highlights sudden changes in the seismic waveforms such as those encountered at channel margins and along faults. The green arrows indicate channel or tributary margins which have been enhanced, and the yellow arrows indicate subtle, previously overlooked faults which can now be detected. The northeast-southwest trending acquisition footprint becomes more prominent with decreasing depth……...……27

Figure 13. Corendered k_1 and k_2 curvature and Sobel filter along each unconformity. K_1 curvature highlights convex seismic reflectors (levees and foot walls of normal faults), and k_2 curvature highlights concave seismic reflectors (channel thalwegs and hanging walls of normal faults). The red and yellow arrows indicate levees and normal fault foot walls, respectively. The blue and green arrows indicate channel thalwegs and normal fault hanging walls, respectively. The northeast-southwest trending acquisition footprint becomes more prominent with decreasing depth……...……29

Figure 14. Corendered valley shape and Sobel filter along each unconformity. The attribute highlights seismic reflectors which are valley-shaped (i.e., channels and scours). The green arrows indicate channel or tributary thalwegs which have been enhanced, and the yellow arrows indicate

erosive scours. The northeast-southwest trending acquisition footprint becomes more prominent with decreasing depth…….……30

Figure 15. Corendered PCA (spectrally balanced amplitude, sweetness, valley shape, peak frequency, and peak magnitude) and Sobel filter extracted along each unconformity……...….31

Figure 16. A) Modified from Simms et al. (2007). A regional contour map of the MIS2 unconformity in the northwestern GoM. The red rectangle represents the HR3D boundary, and the MIS2 unconformity lies at 16 mbsf across the survey. B) Modified from Anderson et al. (2016). A regional digital elevation model of the MIS2 unconformity in the northwestern GoM. The red rectangle represents the HR3D boundary, and the MIS2 unconformity lies at 20 mbsf across the survey. These depths closely correspond to the depth of the UUC which lies at 17 mbsf across the HR3D survey. Therefore, the UUC is likely equivalent to the MIS2 unconformity……..36

Figure 17. Modified from Anderson et al. (1992). An interpreted seismic line from Galveston Bay (40 km northeast of the study area). The MIS2 and MIS6 unconformities are interpreted to lie at 11 mbsf and 53 mbsf, respectively. The depth of the MIS6 unconformity closely corresponds to the depth of the MUC which lies at 60 mbsf across the HR3D survey. Therefore, the MUC is likely equivalent to the MIS6 unconformity……37

Figure 18. Seismic inline 195 showing the complete tripartite (LST, TST, and HST) interpretation of the defined sequences. The LUC, MUC, and UUC are correlated to lowstand events, and MFSs are correlated to highstand events on Johnson and Watt (2012)'s sea level curve……...……41

Figure 19. Conceptual relationship between time and sea level cyclicity. Within one first-order cycle (LST, TST, HST, RST, LST), several second-order cycles will occur. Within one

second-order cycle, several third-order cycles will occur. Within one third-order cycle, several fourth-order cycles will occur. Within one fourth-order cycle, several fifth-order cycles will occur. Axes are unitless as the figure is only meant to demonstrate the hierarchy and superimposition of sea level cycle orders……..44

Figure 20. Interpreted horizon slices from the spectrally balanced amplitude volume flattened upon the reference horizon. Horizon slices show valley evolution from 114 to 100 milliseconds. The system begins as a simple meandering channel devoid of dendritic characteristics. Moving shallower, the channel becomes increasingly wide and sinuous and develops a network of dendritic crevasse splays and tributaries. The foot walls and hanging walls of the two major faults are also labeled as indicated by FW and HW, respectively…….46

Figure 21. Demonstration of how sea level fluctuations generally influence valley morphology. During lowstand times, channels are robust as they are dominated by fluvial processes. As sea level rises, channels become flooded as they are dominated by marine processes.……...……..……..48

Figure 22. Corendered PCA and Sobel filter along the MUC. Facies which are typically dominated by coarse-grained sediments are represented by purple colors; red and pink arrows indicate crevasse splays and mid-channel bars, respectively. Facies which are typically dominated by fine-grained sediments are represented by green colors; green and blue arrows indicate floodplain and main channel fill, respectively. In cross-section, crevasse splays exhibit a clear bump which is indicative of sand fill, and the main channel exhibits a clear sag which is indicative of mud fill. Thus, it can be inferred that purple colors correspond to coarse-grained sediments, and green colors correspond to fine-grained sediments…….……..……..49

LIST OF TABLES

Table 1. Calculations of wavelength and vertical resolution; λ = wavelength, v = velocity, f = frequency, and R_V = vertical resolution……..…...11

Table 2. Summary of HR3D seismic data acquisition and display parameters…..…..……11

Table 3. Summary of computed seismic attributes and their use in this study……...……..17

Table 4. Summarized from Vail et al. (1977), Mitchum et al. (1990), and Goldhammer et al. (1990). Sea level cycle order hierarchy and their typical sequence thickness, sea level amplitude, duration, sea level rise and fall rates, and cause…….…….42

ABSTRACT

Resolution limitations of conventional seismic methods prohibit the subsurface investigation of high-frequency—fourth and fifth-order—depositional sequences and their associated fluvial features. However, modern high-frequency 3D seismic methods provide sufficient resolution for such analyses. This study utilized high-resolution 3D seismic data to investigate Quaternary high-frequency depositional sequences and incised valley evolution on the northwestern Gulf of Mexico's inner shelf. Within the shallowest 200 milliseconds of the subsurface, three major unconformities were identified and mapped. Through a seismic attribute analysis and the employment of machine learning algorithms, fluvial features along each unconformity—likely related to the Brazos and/ or Trinity Rivers—were delineated and determined to be incised valleys which are known to have formed during eustatic lowstand events. Using a tripartite seismic stratigraphic scheme, systems tracts—lowstand systems tracts, transgressive systems tracts, and highstand systems tracts—were identified within each defined sequence, and sequence boundaries (i.e., unconformities) were correlated to lowstand events on a eustatic sea level curve. Incised valley evolution was then investigated which revealed that such systems maintain a tendency to become increasingly sinuous and dendritic in response to rapid transgression. Finally, various seismic attributes were employed in a principal component analysis which facilitated an understanding of lithologic distribution throughout the seismic volume. This study underscores the significance of high-resolution seismic data, seismic attributes, and machine learning in understanding high-frequency sea level cycles and provides insight into Late Quaternary depositional processes on the Gulf of Mexico's inner shelf. Knowledge of these high-frequency depositional sequences in the shallow subsurface may aid in understanding the small-scale

heterogeneity of deeper reservoirs where such features are unresolvable through conventional seismic methods.

INTRODUCTION

The Gulf of Mexico (GoM) is a petroliferous, ocean basin located between the eastern coast of Mexico and the southern coast of the United States. Quaternary fill in the GoM provides a continuous record of depositional processes over the past 2.6 million years. On the inner shelf, much of this fill records eustatic sea level fluctuations and the subsequent geomorphological evolution of North American fluvial systems such as the Tennessee, Mississippi, Red, Trinity, Brazos, Colorado, and Rio Grande Rivers (Galloway et al., 2011).

In the subsurface, sequence stratigraphy and fluvial channel evolution is best understood through 3D seismic data. Conventional 3D seismic data is recorded with large bin sizes of 25 x 25 meters and at low frequencies of 10 to 80 Hz which results in approximate horizontal and vertical resolutions of 25 meters and 10 to 20 meters, respectively (Souza et al., 2019). Due to these resolution limitations, conventional seismic data is often unable to image high-frequency depositional sequences and small-scale fluvial features such as those related to the Brazos and Trinity Rivers. Thus, such geologic features must be investigated using high-resolution 3D (HR3D) seismic data.

In 2013, to explore potential carbon dioxide storage sites, researchers at the University of Texas recorded a shallow HR3D seismic survey south of San Luis Pass, Texas. The HR3D survey was recorded with a bin size of 6.25 x 6.25 meters and at high frequencies of 50 to 250 Hz which resulted in a horizontal resolution of 6.25 meters and a vertical resolution of 2.24 meters. Therefore, the HR3D dataset provides a unique opportunity to evaluate and better understand high-frequency sea level cycles and the evolution of small-scale fluvial systems throughout the study area.

Meckel and Mulcahy (2016) first used the volume to evaluate the evolution of previously unresolvable Quaternary channels related to the Brazos River. Furthermore, their study primarily focused upon the comparison of channel geomorphology along two shallow unconformities. Through the application of seismic attributes and unsupervised machine learning algorithms, this study explores remaining questions regarding the two previously mapped unconformities and their sequence stratigraphic framework. Additionally, to gain a more comprehensive understanding of the GoM's Quaternary sea level fluctuations and channel evolution, a deeper unconformity is also investigated. Because HR3D seismic coverage is highly limited, enhanced knowledge of high-frequency depositional sequences and channel evolution in this area may aid in understanding the vertical and lateral distribution of similar, seismically unresolvable Cenozoic deposits throughout the GoM.

GEOLOGICAL BACKGROUND

To best understand the geologic features within the HR3D volume, it is important to first comprehend the broader-scale processes which have influenced the San Luis Pass area. Therefore, this section will cover the GoM's regional geologic history prior to delving into its Quaternary inner shelf geology.

Regional Basin Evolution

The precise details of Mesozoic rifting and subsequent development of oceanic crust in the GoM remain a subject of ongoing debate. However, a broad consensus exists among previous researchers regarding the key phases of the basin's tectonic evolution. In the Late Triassic, initial subsidence was instigated by the northwest-southeast oriented continental rifting of Pangea (Martini and Ortega-Gutiérrez, 2018). With continued crustal extension, a brief period of widespread syn-rift salt deposition transpired in the Middle to Late Jurassic. Finally, in the Latest

Jurassic, prolonged rifting led to the complete development of an ocean basin characterized by seafloor spreading and transform faulting which resulted in a counterclockwise rotation of the Yucatan Block and ultimately led to the configuration of the modern-day GoM (Garcia-Reyes and Dyment, 2022). Seafloor spreading concluded in the Early Cretaceous—the time at which the northern GoM transitioned into a passive margin. However, due to cooling of the lithosphere and rapid sedimentation, subsidence along the basin's northern margin continued into the Cenozoic (Martini and Ortega-Gutiérrez, 2018).

Inner Shelf Quaternary Geology and Sea Level Changes

In recent geologic history, sedimentation in the northwestern GoM has been dominated by siliciclastic processes as siliciclastic sediments of North American provenance have been transported to the basin by numerous north-south-trending fluvial systems such as the Tennessee, Mississippi, Red, Trinity, Brazos, Colorado, and Rio Grande Rivers (Galloway et al., 2011). During the Pleistocene, these fluvial systems contributed significantly to the deposition of nearly four kilometers of sediments at a considerable rate of approximately 240 centimeters per year (Xie et al., 2017). Throughout the Pleistocene, the geomorphology of the aforementioned fluvial systems was everchanging due to a complex interplay of dynamic factors—eustatic sea level, subsidence rates, sediment supply, and climate. While all of these factors undoubtedly influenced fluvial geomorphological evolution, it is probable that the most substantial impact arose from highly variable eustatic sea levels which have fluctuated by more than 130 meters over the past 400,000 years (Johnson and Watt, 2012).

Due to the shallow focus of this study, it is critical to possess a thorough understanding of these recent—<400,000 years to present—sea level fluctuations. In a previous study, Johnson and Watt (2012) constructed an average Late Quaternary eustatic sea level curve from worldwide findings

by Wright (2000), Waelbroeck et al. (2002), and Peltier (2005). These curves were estimated from oxygen isotopes of benthic and planktic foraminifera in the Caribbean Sea and Atlantic, Pacific, and Indian Oceans which indicate changes in global ice volume (Simms et al., 2007).

The sea level curve constructed by Jonson and Watt (2012) exhibits sea level falls which tend to be slow and intermittent and sea level rises which tend to be rapid and continuous. Moreover, within the last 400,000 years, there have been five major highstand events which coincide with interglacial periods—times at which global temperatures were warm, and global ice volumes were low. Additionally, there have been four major lowstand events which coincide with glacial periods—times at which global temperatures were cool, and global ice volumes were high (Figure 1). In general, these lowstand events correspond to the Nebraskan, Kansan, Illinoian, and Pre-Illinoian North American land glacial stages (Gibbard and Cohen, 2008; Pigott et al., 2011). During each lowstand event, fluvial systems underwent requisite adjustments to accommodate reductions in base level which led to the progradation of channels across the subaerially exposed inner shelf. This progradation gave rise to the development of complex incised valleys which were filled with estuarine sediments during the late lowstand phase (Meckel and Mulcahy, 2016).

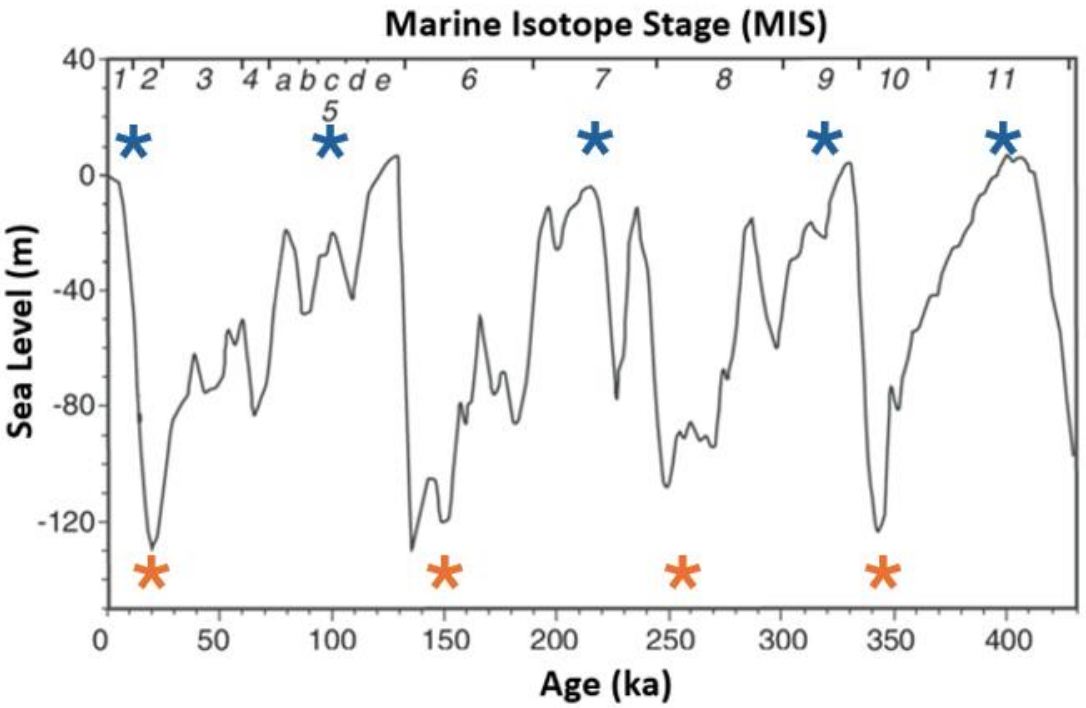

Figure 1: Modified from Johnson and Watt (2012). Late Quaternary eustatic sea level curve spanning from present to 400,000 years. In this span of time, five highstand events (blue asterisks) and four lowstand events (orange asterisks) occurred.

Brazos and Trinity River Systems

Due to the proximity of the study area to the modern-day and paleo Brazos and Trinity River outlets, the valley incisions throughout the interval of interest are ascribed primarily to the Brazos and Trinity River systems. Thus, it is critical to grasp a basic understanding of these rivers prior to delving into this study.

Originating in New Mexico, the Brazos River extends over 1,900 kilometers and traverses most of Texas' principal physiographic regions (Yao et al., 2022). Today, the Brazos River drains an area of 118,000 km^2 and enters the GoM near Freeport, Texas where it exhibits an average annual discharge of 7,246,000 acre-feet per year (Yao et al., 2022; Wurbs and Zhang, 2016). Originating in northern Texas, the Trinity River extends approximately 1,136 kilometers and traverses most of Texas' principal physiographic regions. Today, the Trinity River drains an area of 40,000 km^2 and

enters Galveston Bay near Liberty, Texas where it exhibits an annual discharge of 6,630,000 acre-feet per year (Yao et al., 2022; Wurbs and Zhang, 2016).

Study Area Geology

The HR3D seismic volume encompasses several characteristic features of the northern GoM (Figure 2). For instance, a sizeable salt diapir exists in the northeast portion of the survey. The salt structure vertically extends nearly the entire record length—50 to 1,600 milliseconds—and exhibits a lateral diameter of approximately 1,700 meters at its maximum. The northwest margin of the diapir is bounded by a large northwest-southeast trending normal fault. Additionally, due to rapid sedimentation in the area, several northeast-southwest oriented normal growth faults exist in the southwest portion of the survey. For simplification, throughout this analysis, the large, salt bounding, northwest-southeast oriented fault will be referred to as the Salina Fault, and the northeast-southwest oriented growth faults will be referred to collectively as the Incrementum Faults. A large gas chimney previously described by Meckel and Mulcahy (2016) is also present in the southwest portion of the survey. Finally, and most importantly, throughout the shallowest 200 milliseconds of the HR3D volume, there are several major unconformities. These erosional surfaces and their associated depositional sequences will be the primary focus of this thesis.

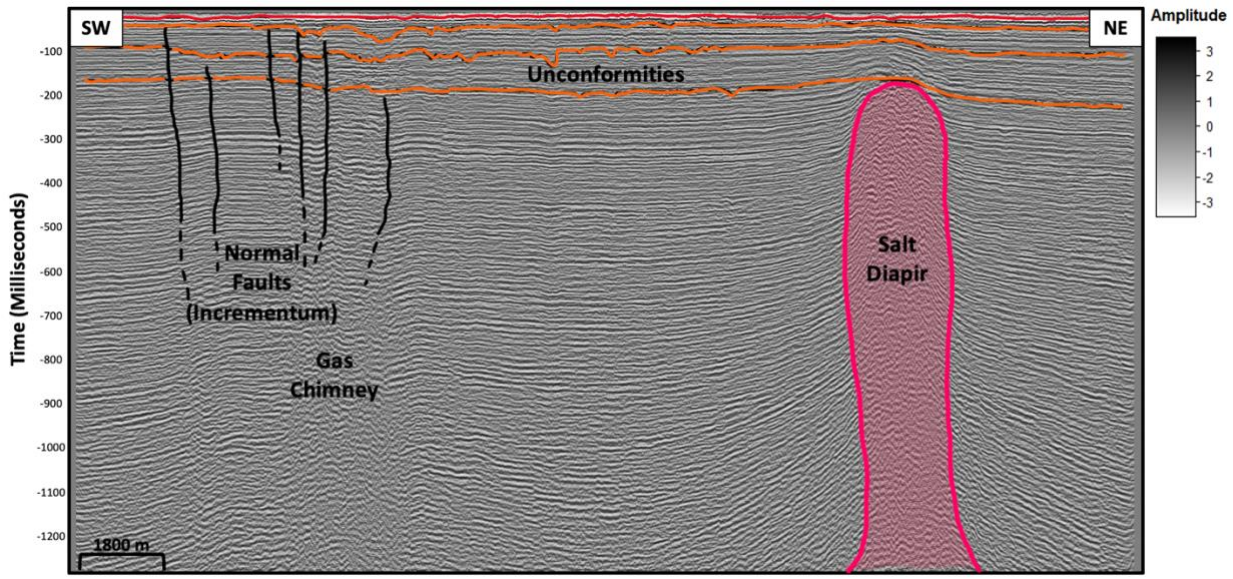

Figure 2: Seismic inline 230 showing the major geologic elements as also identified by Meckel and Mulcahy (2016) within the HR3D volume. The survey encompasses several common GoM features—salt (pink), normal faults (black), unconformities (orange), sea floor (red) etc.

DATA

While oil and gas wells exist within the seismic boundary, no publicly available well data—logs or core—is present through the interval of interest due to its extremely shallow depth of 0 to 125 meters. Consequently, this study relied chiefly upon the HR3D seismic data.

Limitations of Conventional 3D Seismic Data

Seismic resolution is crucial in geophysical investigations as it determines the ability to distinguish subsurface features. While vertical resolution is influenced by numerous factors, wavelength asserts the most direct impact. Moreover, with decreased wavelength, vertical resolution is improved. However, to achieve shortened wavelength, wave frequency must be increased. High-frequency acoustic waves lack practicality as they are easily attenuated and unable to reach adequate depths for most subsurface analyses—hydrocarbon exploration, basement characterization, etc. Because these studies require deep penetration of the acoustic waves, conventional 3D seismic surveys are recorded at low frequencies—10 to 80 Hz—resulting in a

vertical resolution of 10 to 20 meters (Souza et al., 2019). Like vertical resolution, horizontal resolution is also influenced by numerous factors, but bin size asserts the most direct impact. Conventional 3D seismic surveys are recorded with large bin sizes—25 x 25 meters—which results in poor lateral resolution. Furthermore, in shallow waters, such as those overlying the study area, the large bin sizes of conventional seismic surveys prohibit imaging of the shallowest subsurface—< 500 milliseconds—due to muting of the data in processing (Figure 3). As a result, publicly available conventional seismic data in the GoM is unable to sufficiently image shallow, high-frequency depositional sequences (i.e., fourth and fifth order) and shallow features related to small-scale Texas fluvial systems such as the Brazos and Trinity Rivers.

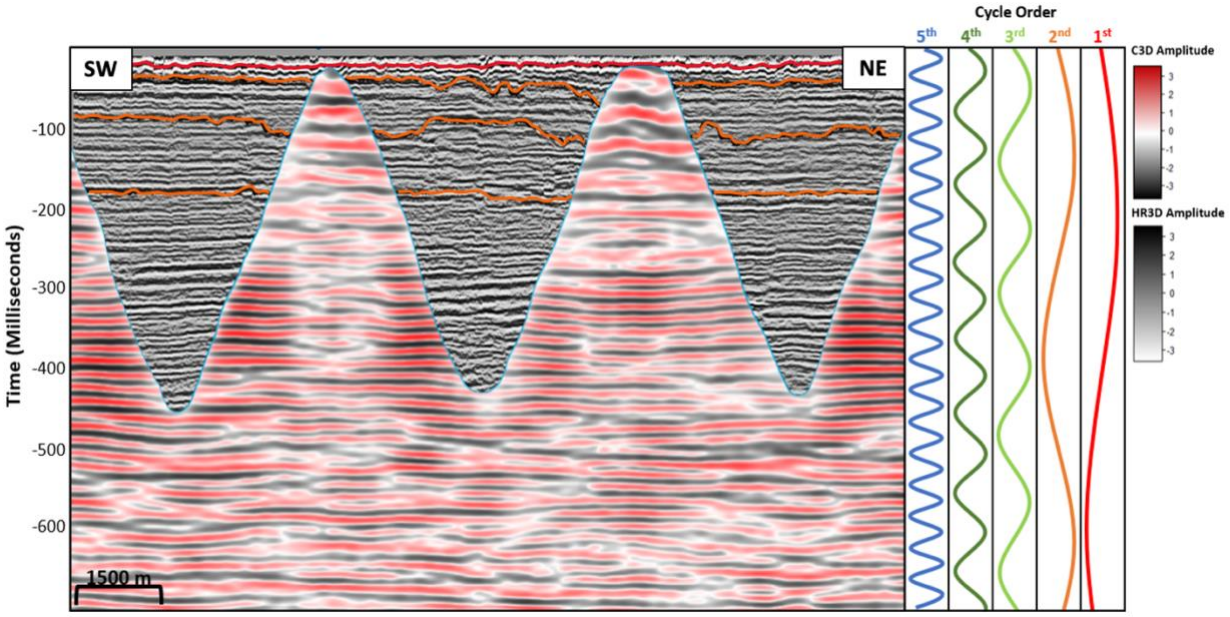

Figure 3: Comparison of high-resolution 3D (HR3D) seismic (peak frequency = 130 Hz) to conventional 3D (C3D) seismic (peak frequency = 40 Hz) from the San Luis Pass area. To the right, the sea level curves are vertically scaled to the average thickness—in this case, time—of their stated depositional sequences (first, second, third, fourth, and fifth). Due to shallow water depths and large bin sizes, important data is muted throughout the shallowest 475 ms of the C3D volume (i.e., the interval of interest). Additionally, while fourth and fifth order sequences may appear within the C3D volume as single peaks or troughs, the resolution is not sufficient for a seismic stratigraphic analysis of the sequences. In contrast, no important data is muted within the HR3D volume, and the vertical resolution permits the analysis of fourth and fifth order depositional sequences.

HR3D Seismic Survey

For the aforementioned reasons, in 2013, researchers employed a P-Cable high-resolution 3D system to record the HR3D seismic survey near the present-day Brazos River Delta south of San Luis Pass, Texas in water depths of 14 to 15 meters. Further, the seismic polygon measures 2.3 km x 12.5 km and encompasses approximately 29 km^2 as it trends parallel to the shoreline in the northeast-southwest direction (Figure 4). The dataset was recorded using a small bin size of 6.25 x 6.25 meters and at high frequencies ranging from approximately 50 to 250 Hz. This combination of small bin size and high frequency content permitted ample imaging of the shallowest subsurface without loss of information to muting. Due to the attenuation of the high-frequency waves, the processed record length extends to only 1,600 milliseconds. However, for the purpose of this study, this did not pose an issue as the interval of interest is very shallow—0 to 200 milliseconds.

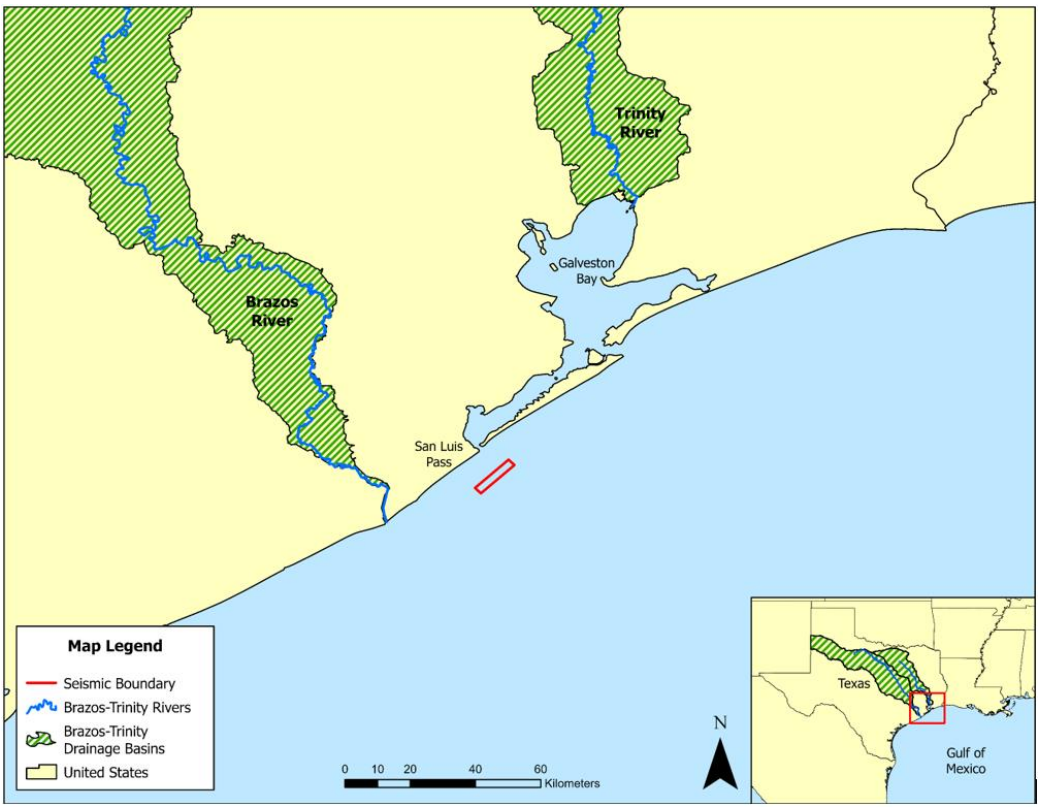

Figure 4: Geographic location of the study area located~16 km south of San Luis Pass, Texas indicated by the red polygon. The HR3D seismic survey covers a small area of 29 km2.

HR3D Seismic Resolution

In order to calculate the vertical resolution of the HR3D seismic data, wave frequency and velocity must be known. It was first determined that the dominant frequency through the interval of interest was 130 Hz (Appendix A). Due to the absence of well data necessary for a precise time-to-depth conversion, it was not possible to obtain an exact value for wave velocity. However, in the 1990s, Exxon recorded check-shot surveys at three wells in the GoM's upper slope and obtained average velocities of 1,504 m/s, 1,525 m/s, and 1,547 m/s down to 150 meters below the seafloor. Because our interval of interest lies between 0 and 125 meters in the subsurface, these check-shot surveys provide a sufficient average velocity value of 1,525 m/s for this analysis. In a similar study which focused on adjacent areas, Abdulah et al. (2004) used this same sediment velocity value for estimating depths of stratigraphic packages and identifying unconformities in high-resolution 2D seismic data and presented positive findings. Therefore, using a frequency value of 130 Hz and velocity value of 1,525 m/s, the vertical resolution through the interval of interest was derived through use of the equations in Table 1.

Wavelength	**Vertical Resolution**
$\lambda = v / f$ ↓ $\lambda = 1{,}525 / 130$ ↓ **11.73 meters**	$R_V = \lambda / 4$ ↓ $R_V = 11.73 / 4$ ↓ **2.93 meters**

Table 1: Calculations of wavelength and vertical resolution; λ = wavelength, v = velocity, f = frequency, and R_V = vertical resolution.

With the ability to vertically resolve features as small as 2.93 meters and laterally resolve features as small as 6.25 meters, the HR3D dataset exhibits resolution which is four to ten times better than that of conventional 3D seismic data.

Acquisition Date	2013
Coverage	29 km^2
Bin Size	6.25 x 6.25 m
Dominant Frequency	130 Hz
Sample Interval	0.5 ms
Record Length	1,600 ms
Phase	90°

Table 2: Summary of HR3D seismic data acquisition and display parameters.

METHODS

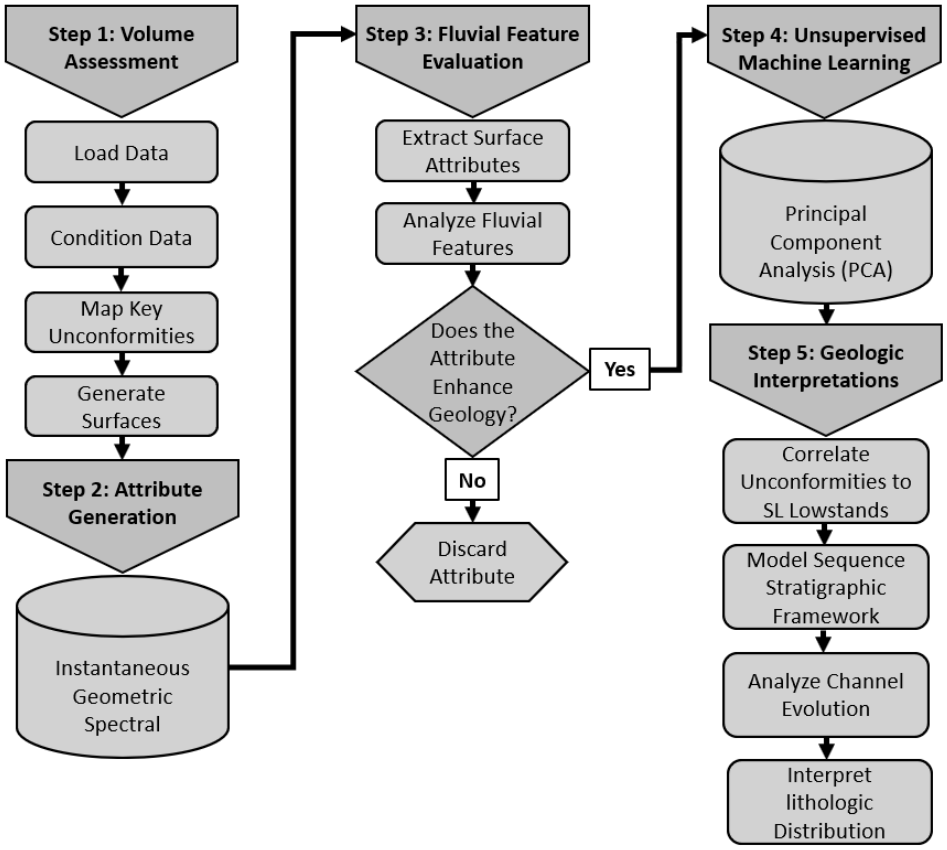

Figure 5: The implemented workflow for this study.

Data Loading and Conditioning

The HR3D dataset was first retrieved from the Marine Geoscience Data System in the form of a SEG-Y file which was then imported into an interpretation application for a preliminary inspection. Given the high frequency content of the volume, the shallowest section exhibited a strong northeast-southwest trending acquisition footprint and was characterized by a low signal-to-noise ratio. Thus, it was determined that further data conditioning was required. Through a conservative conditioning method, the acquisition footprint was drastically reduced, and the overall signal-to-noise ratio was optimized without sacrificing any geological information. After suppressing the acquisition footprint, the HR3D volume was spectrally balanced which helped to

further enhance the definition of geologic features and led to improved interpretability. To expedite attribute computations, the volume was then cropped from 0 to 400 milliseconds reducing the size—and ultimately attribute computation time—of the original HR3D volume by approximately 75%.

Unconformity Identification and Mapping

Upon achieving a satisfactory standard of data quality, interpretations of erosional unconformities were made. Vail et al. (1977) define an unconformity as "a surface separating younger from older strata, along which there is evidence of subaerial erosional truncation (and, in some areas, correlative submarine erosion) or subaerial exposure, with a significant hiatus indicated." Using this logic, in the shallowest 200 milliseconds of the volume, three major unconformities were identified through the recognition of truncated reflectors (Figure 6). In order from oldest to youngest, the unconformities were assigned names of Lower Unconformity (LUC), Middle Unconformity (MUC), and Upper Unconformity (UUC).

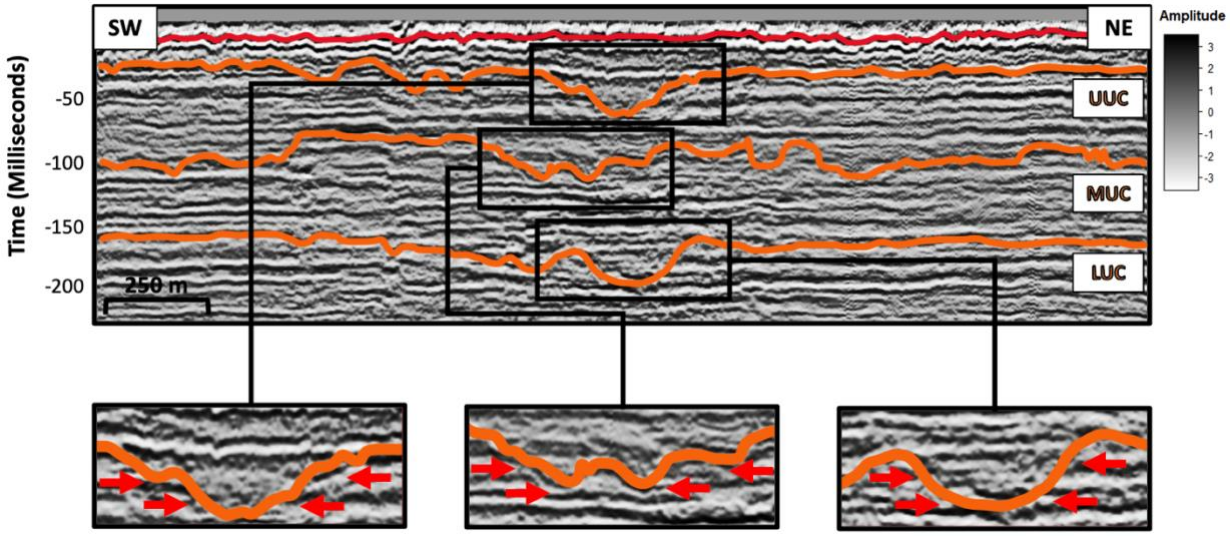

Figure 6: Interpreted unconformities along seismic inline 195. The unconformities were assigned names of Lower Unconformity (LUC), Middle Unconformity (MUC), and Upper Unconformity (UUC). Each unconformity is characterized by the lateral truncation of seismic reflectors as indicated by red arrows.

To enhance the visibility of the erosional surfaces, prior to mapping, a greyscale color scheme was applied to the amplitude volume. Beginning with the UUC, interpretations were made along numerous arbitrary lines oriented perpendicular to the structural fabric; this method ensured accurate correlation of the unconformity across faults. Next, through the use of a conventional loop-tying technique, the erosional surface was mapped to the extent of the seismic boundary. This general workflow was also implemented in mapping the MUC and LUC. However, due to extreme distortion of the data caused by the gas chimney in the southwest portion of the survey, a small area—1.6 km^2—of the LUC was unable to be mapped with confidence and was therefore avoided. Once the unconformities were mapped thoroughly, a convergent interpolation algorithm was employed to generate time-structure maps from the three horizons.

Unconformity Time-to-Depth Conversions

After analyzing the statistics of each surface, it was determined that the Lower, Middle, and Upper Unconformities lie at mean two-way travel times (TWT) of 166, 98, and 42 milliseconds, respectively. It was also determined that the seafloor lies at approximately 19 milliseconds. Using these values and Exxon's predetermined interval velocity of 1,525 m/s, subsurface depths of each unconformity were estimated through the use of the following equation.

$$\mathbf{SD_{UC} = [(TWT_{UC} - TWT_{SF}) \times V_{AVG}] / 2}$$

Where:

SD_{UC} = Subsurface depth of unconformity (meters)

TWT_{UC} = Two-way travel time at unconformity (seconds)

TWT_{SF} = Two-way travel time at sea floor (seconds)

V_{AVG} = Average interval velocity (meters per second)

This revealed that the LUC lies at an approximate depth of 112 meters below the seafloor (mbsf); the MUC lies at an approximate depth of 60 mbsf, and the UUC lies at an approximate depth of 17 mbsf.

Seismic Attributes

To aid in the visualization and interpretation of geological features along each unconformity, various seismic attributes were derived from the HR3D volume. For this study, attributes which are specifically known to enhance fluvial channels and their associated architectural elements were calculated such as Sobel filter, sweetness, and more. The following paragraphs will explain each of the computed attributes and their relevance to this study.

Spectrally Balanced Amplitude

Chopra and Marfurt (2016) describe spectral balancing as an algorithm which takes the processed input data and generates as flat of a spectrum as the signal-to-noise ratio permits without altering the phase spectrum. As a result, the amount of noise throughout the data is drastically reduced, and resolution is improved. For these reasons, spectral balancing aids tremendously in improving the quality and interpretability of seismic data—especially in high-frequency datasets such as the HR3D survey.

Sweetness

Radovich and Oliveros (1998) define sweetness as the instantaneous amplitude divided by the square root of instantaneous frequency and first used the attribute upon the recognition that sand-rich facies embedded in a shale matrix often exhibit lower instantaneous frequency and higher envelope. Thus, high sweetness values are often indicative of sand-rich facies which may potentially be saturated with hydrocarbons—hence, the term “sweetness”. While this attribute is highly useful in delineating facies distribution, its effectiveness is not uniform across all

depositional settings. Moreover, sweetness is not as effective in delineating facies in areas which lack strong lithologic contrasts such as fine-grained channel sands encased by fine-grained floodplain sediments. Rather, it is most effective in delineating facies in areas where strong lithologic contrasts are present such as coarse-grained channel sands encased by fine-grained floodplain sediments.

Sobel Filter

Lou et al. (2003) describe Sobel filter as the magnitude of the inline and crossline derivatives of seismic amplitude along structural dip. Simply put, Sobel filter attribute detects sudden changes in the amplitude values. For this reason, Sobel filter is great at highlighting geologic features which are characterized by discontinuities or sudden changes in lithology such as faults and channel margins, respectively.

Most-Positive (K_1) Curvature and Most-Negative (K_2) Curvature

Roberts (2001) describes the principal curvatures k_1 and k_2 as the inverse of radii of curvature that best fit the local structure. Simply put, most-positive curvature detects positive curvedness of seismic reflectors throughout the data. Thus, k_1 curvature is great at highlighting geologic features which are characterized by convex reflectors such as the foot wall of normal faults, channel margins, and levee deposits. Similarly, most-negative curvature detects negative curvedness of seismic reflectors throughout the data. Thus, k_2 curvature is great at highlighting geologic features which are characterized by concave reflectors such as the hanging wall of normal faults and channel thalwegs. Although k_1 and k_2 curvature are useful when used independently, the attributes are immensely useful when they are corendered with one another.

Valley Shape

Al-Dossary and Marfurt (2006) describe shape index as an attribute which uses the principal components of k_1 and k_2 curvature to define local structure as either a dome, bowl, saddle, valley, ridge, or plane. Furthermore, if the shape index value of the seismic reflector equals -0.5, the attribute classifies the structure as a valley. Thus, as the name implies, valley shape excels at highlighting "valley-shaped" seismic reflectors such as those associated with channel bases and scours.

Attribute	**Use**
Spectrally Balanced Amplitude	Identification of general geologic features (i.e., channels, faults, salt, etc.)
Sweetness	Identification of general geologic features and delineation of lithologic distribution (i.e., sand vs. shale)
Sobel Filter	Identification of channel edges and faults
K_1 Curvature	Identification of channel edges (i.e., levee deposits)
K_2 Curvature	Identification of channel bases (i.e., thalwegs)
Valley Shape	Identification of channel bases and erosive scours

Table 3: Summary of computed seismic attributes and their use in this study.

Upon successful computation of the above-mentioned attributes, the output attribute volumes were examined for quality. The values of each attribute were then extracted along the three unconformities, and the color bars of each attribute volume were altered to best portray the results.

Sequence Stratigraphy

Following the assessment of the attribute volumes, stratigraphic interpretations were made throughout the interval of interest. Furthermore, a tripartite scheme like that applied by Pigott et al. (2011) in the Gulf of Thailand, which involved the identification of transgressive and maximum

flooding surfaces, was implemented in subdividing each of the defined sequence into lowstand systems tracts (LSTs), transgressive systems tracts (TSTs), and highstand systems tracts (TSTs). The sequence stratigraphic model was constrained to the findings of similar nearby studies and, most importantly, to the sea level curve from Johnson and Watt (2012). Channel evolution in response to fluctuating sea level was then investigated along the unconformities which preserved such phenomena—specifically the MUC.

Valley Evolution

While the surface attributes permitted the static interpretation of fluvial features along each individual unconformity, an alternate strategy was required to analyze the evolution of channels through time. Unfortunately, due to the structural complexity of the study area, conventional time slices did not adequately depict channel evolution. Thus, to mitigate this issue, a reference horizon, which approximately paralleled stratigraphy and properly crossed faults, was mapped. Finally, certain attribute volumes were flattened on the reference horizon which allowed for channel evolution to be investigated. Moreover, channel evolution along the MUC was observed and interpreted by moving vertically through the flattened spectrally balanced amplitude volume.

Machine Learning

The absence of well data through the interval of interest renders an incomplete understanding of lithologic distribution throughout the HR3D volume. In recent seismic analyses, authors have delineated lithologic variations through unsupervised machine learning techniques (Celecia et al., 2021). Therefore, to gain a better understanding of lithologic distribution along each unconformity, various combinations of seismic attributes were employed in unsupervised machine learning algorithms. At first, numerous combinations of only the previously mentioned attributes—spectrally balanced amplitude, Sobel filter, sweetness, k_1 curvature, k_2 curvature, and valley

shape—were tested. However, superior results were derived when spectral attributes such as peak frequency and peak magnitude were incorporated. Although these spectral attributes were not immensely helpful when used independently (Appendices B and C), their significance became pronounced when integrated into a comprehensive suite of attributes. Moreover, the best combination of attributes was determined to be spectrally balanced amplitude, sweetness, valley shape, peak frequency, and peak magnitude. This combination of attributes yielded the most favorable results in a principal component analysis (PCA). Previous authors employed seismic attributes in a PCA to explore lithologic distribution across various depositional environments and presented positive findings (Hu et al., 2017).

Principal Component Analysis (PCA)

Zhao et al. (2015) describe PCA as an algorithm which reduces the redundancy and dimensionality of the input attribute data. Moreover, PCA first works to find a new orthogonal coordinate system which best represents the data variation; the data is then projected onto this new coordinate system. By doing so, the number of dimensions is reduced, and the data is clustered according to similarities between the input attributes—in this case, spectrally balanced amplitude, sweetness, valley shape, peak frequency, and peak magnitude. As a result, PCA is often able to provide valuable insight into lithologic properties. Importantly, while lithology may be inferred from PCA, it should be noted that the algorithm alone may not achieve an exact delineation of lithology due to its inherent limitations.

RESULTS

Data Conditioning and Spectral Balancing

Through the conservative filtering approach, the acquisition footprint was drastically reduced, and the overall signal-to-noise ratio was enhanced. Because geometric attributes best portray the

severity of the acquisition footprint, Sobel filter was used in determining optimal noise filtering parameters and therefore best communicates the results. While the entire HR3D volume was improved, substantial reduction of the acquisition footprint can specifically be seen in the survey's southwest portion as indicated by green arrows in Figure 7. Most importantly, no geological information appears to have been compromised. In fact, geologic features such as faults and channel margins appear to be enhanced throughout much of the filtered volume. These enhancements are indicated by blue arrows in Figure 7.

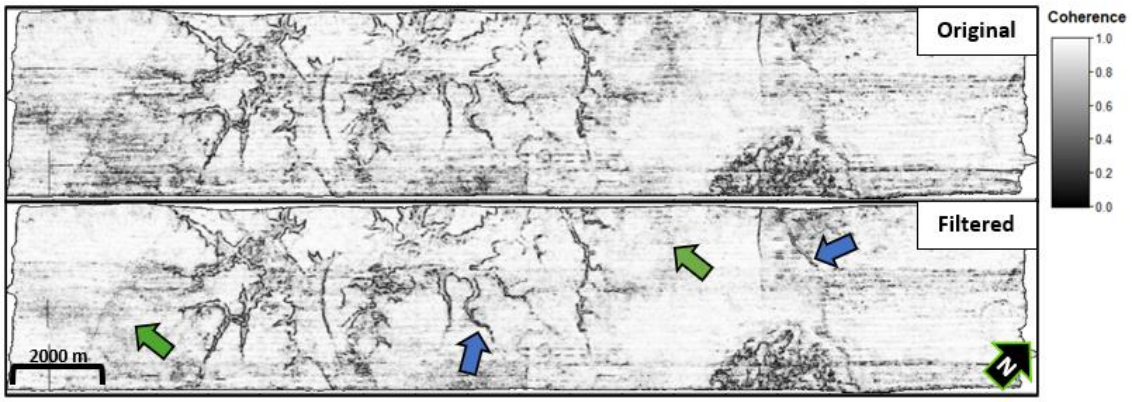

Figure 7: Comparison of the original vs. filtered data using the Sobel filter attribute along a time slice of 0.05 seconds. Green arrows indicate areas where the filtered volume demonstrates reduced acquisition footprint, and blue arrows indicate areas where the filtered volume demonstrates enhanced geologic features.

By achieving spectral balance throughout the HR3D amplitude volume, remaining noise was filtered, and seismic resolution was improved. This resulted in improved visualization and interpretability of fluvial features and structural elements throughout the survey. In comparison to the original amplitude volume, the spectrally balanced volume exhibits a clearer definition of channel margins and associated architectural elements such as crevasse splays, point bars, and channel bars as indicated by green arrows in Figure 8. Henceforth, the spectrally balanced amplitude volume was utilized in lieu of the original amplitude volume throughout this analysis.

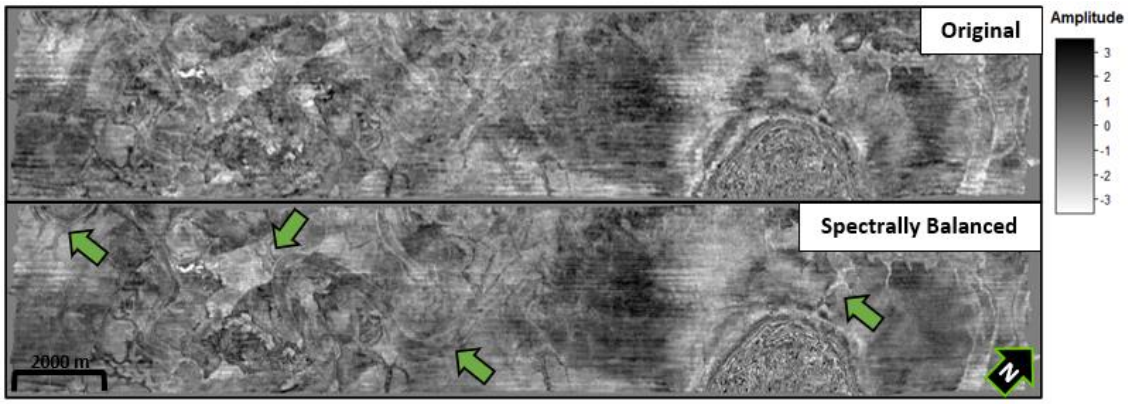

Figure 8: Comparison of the original vs. spectrally balanced amplitude along a time slice of 0.11 seconds. The spectrally balanced volume exhibits a further enhanced signal-to-noise ratio and improved resolution. The green arrows indicate channel margins and architectural elements which are more well-defined along the spectrally balanced time slice.

Unconformity Time-Structure Maps

The time-structure maps generated from the three horizons revealed insightful and fundamental information regarding each unconformity. Most importantly, the time-structure maps exposed the major fluvial features along each unconformity, but these maps were also instrumental in highlighting and understanding the major structural elements throughout the HR3D volume. When used independently, the time-structure maps do not adequately depict shallow fluvial features and subtle structural elements. To mitigate this issue, these maps were corendered with the spectrally balanced amplitude volume.

The corendered time-structure and amplitude map of the LUC unveiled a south-trending channel accompanied by numerous dendritic tributaries. The main channel varies in width from 120 to 290 meters and exhibits a maximum incision of 33 meters. Due to its depth, the LUC demonstrates the most significant structural deformation by the salt diapir and is also notably affected by the Salina Fault and Incrementum Faults. Moreover, at the LUC's depth, the Salina Fault exhibits a maximum

throw of 48 meters, and the Incrementum Faults exhibit maximum throws ranging from 7 to 25 meters.

The corendered time-structure and amplitude map of the MUC unveiled a large, moderately sinuous, south-trending, meandering channel accompanied by a complex network of dendritic tributaries and crevasse splays. The main meandering channel varies in width from 150 to 380 meters and exhibits a maximum incision of 42 meters. Additionally, the sinuosity of the channel—channel length divided by valley length—was measured to be 2.68. Like the LUC, the MUC demonstrates structural deformation by the salt diapir and is also affected by the Salina Fault and Incrementum Faults. At the MUC's depth, the Salina Fault exhibits a maximum throw of 29 meters, and the Incrementum Faults exhibit maximum throws ranging from 6 to 11 meters.

Lastly, the corendered time-structure and amplitude map of the UUC revealed a highly dendritic incision in the center of the study area. This incision consists of a main channel accompanied by numerous dendritic tributaries. The main channel varies in width from 250 to 440 meters and exhibits a maximum incision of 43 meters. Due to its shallow depth, the UUC exhibits minimal structural deformation by the salt diapir and the Salina Fault and Incrementum Faults. Moreover, at the UUC's depth, the Salina Fault exhibits a maximum throw of only 9 meters, and the Incrementum Faults are either entirely absent or their effects are negligible. In Figure 9, the main channels along each unconformity are indicated by blue arrows, whereas dendritic tributaries and crevasse splays are indicated by green arrows. Additionally, the salt diapir, Salina Fault, and visible Incrementum Faults are indicated by orange, red, and yellow arrows, respectively.

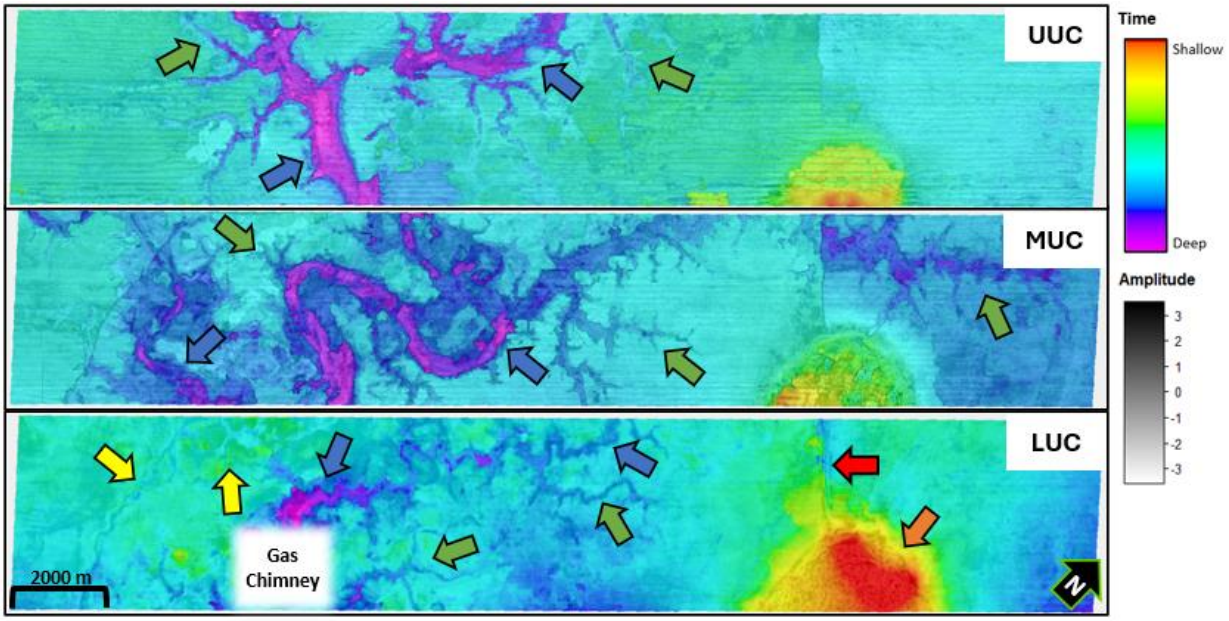

Figure 9: Corendered time-structure and amplitude along each unconformity. The LUC contains a south-trending channel accompanied by numerous dendritic tributaries. The MUC contains a large meandering south-trending channel accompanied by a complex network of dendritic tributaries and crevasse splays. The UUC consists of a main channel accompanied by numerous dendritic tributaries. The blue arrows indicate the main channels, and the green arrows indicate dendritic tributaries and crevasse splays. The orange arrow indicates the salt diapir. The red arrow indicates the Salina Fault, and the yellow arrows indicate the visible Incrementum Faults.

Seismic Attributes

As expected, seismic attributes were pivotal in gaining a deeper understanding of the identified fluvial features, but they also helped to unveil additional features throughout the HR3D volume. Although many attributes were calculated, their performance was not uniform as some proved more adept than others. For example, while geometric attributes such as Sobel filter, most-positive (k_1) and most-negative (k_2) curvatures, and valley shape highlight geology throughout the volume, they also enhance the northeast-southwest trending acquisition footprint—especially at shallow depths (i.e., along the MUC and UUC). Despite the enhanced acquisition footprint, geometric attributes remained useful in delineating fluvial and structural elements. Other attributes such as

amplitude, sweetness, and spectral magnitude also highlight geology throughout the volume and are slightly less impacted by the acquisition footprint.

Spectrally Balanced Amplitude

Previously, spectrally balanced amplitude was discussed in relation to time-structure maps, but the attribute is also insightful when analyzed in isolation. Although the acquisition footprint remained visible in the spectrally balanced amplitude volume, the effects were not overwhelming, and the attribute enabled the identification and evaluation of new geologic features along each unconformity which were not visible within the original amplitude volume. Further, spectrally balanced amplitude was particularly helpful in unveiling shallow, subtle tributaries in the southwest portion of the LUC but also helped in the identification of additional channels along the MUC and UUC as indicated by green arrows in Figure 10. In addition to revealing new channels, the attribute also revealed interesting negative amplitude anomalies throughout the HR3D volume. These anomalies demonstrate amplitude values of -2.0 to -5.5 and exist mostly along the MUC and UUC as indicated by red arrows in Figure 10.

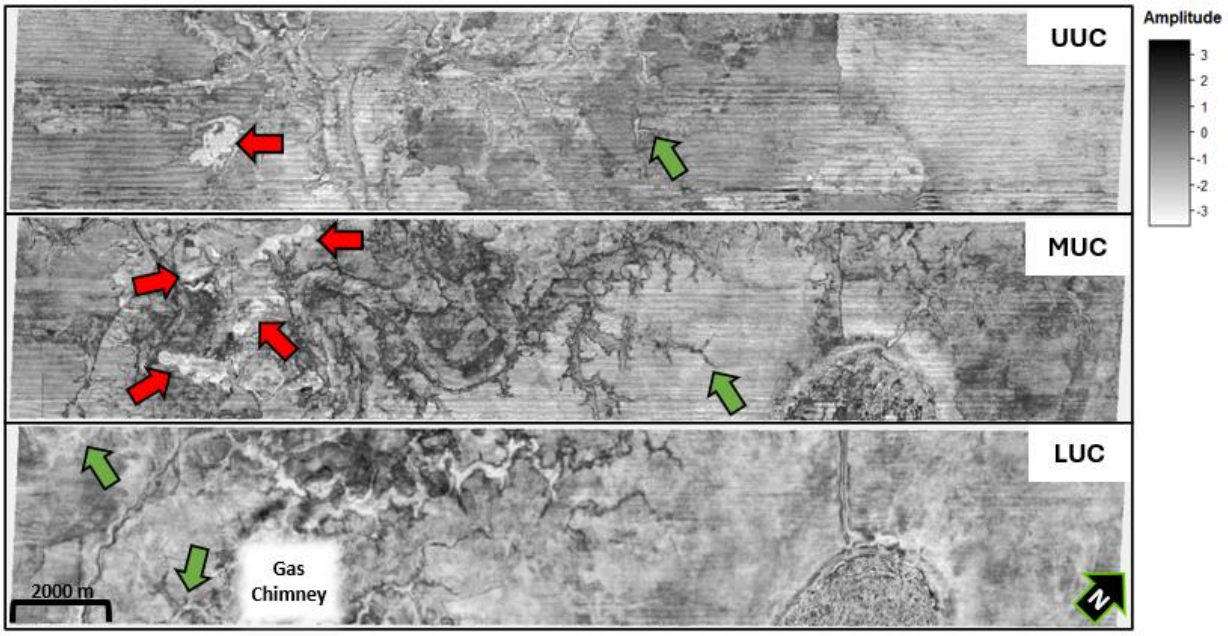

Figure 10: Spectrally balanced amplitude extracted along each unconformity. The attribute permits the visualization of subtle channels and amplitude anomalies throughout the volume. The green arrows indicate subtle channels which were not visible in the original amplitude volume, and the red arrows indicate negative amplitude anomalies. The northeast-southwest trending acquisition footprint becomes more prominent with decreasing depth.

Sweetness

Like spectrally balanced amplitude, sweetness did not significantly enhance the acquisition footprint, and the attribute permitted a deeper understanding of geologic features along each unconformity. Moreover, sweetness helped in further unveiling shallow, subtle channels in the southwest portion of the LUC and revealed additional features along the MUC and UUC as indicated by green arrows in Figure 11. Additionally, due to the absence of well data through the interval of interest, sweetness helped to delineate lithologic distribution along each unconformity as high and low sweetness values are often associated with sands and shales, respectively (Radovich and Oliveros, 1998). The LUC exhibits a wide distribution of sweetness values with higher values—0.25 to 0.45—occurring within and near the main channel and lower values—0.10 to 0.25—occurring throughout the floodplain. The MUC also exhibits a wide distribution of

sweetness values with slightly higher values—0.20 to 0.35—occurring throughout the floodplain and lower values—0.05 to 0.20—occurring within the main channel. With the exception of a few localized areas, the UUC displays generally low sweetness values of 0.05 to 0.20 across its entirety. Additionally, because sweetness is partially derived from amplitude, the attribute also highlighted the previously discussed anomalies along the MUC and UUC. These anomalies are represented by abnormally high sweetness values of 0.80 to 0.95 as indicated by red arrows in Figure 11.

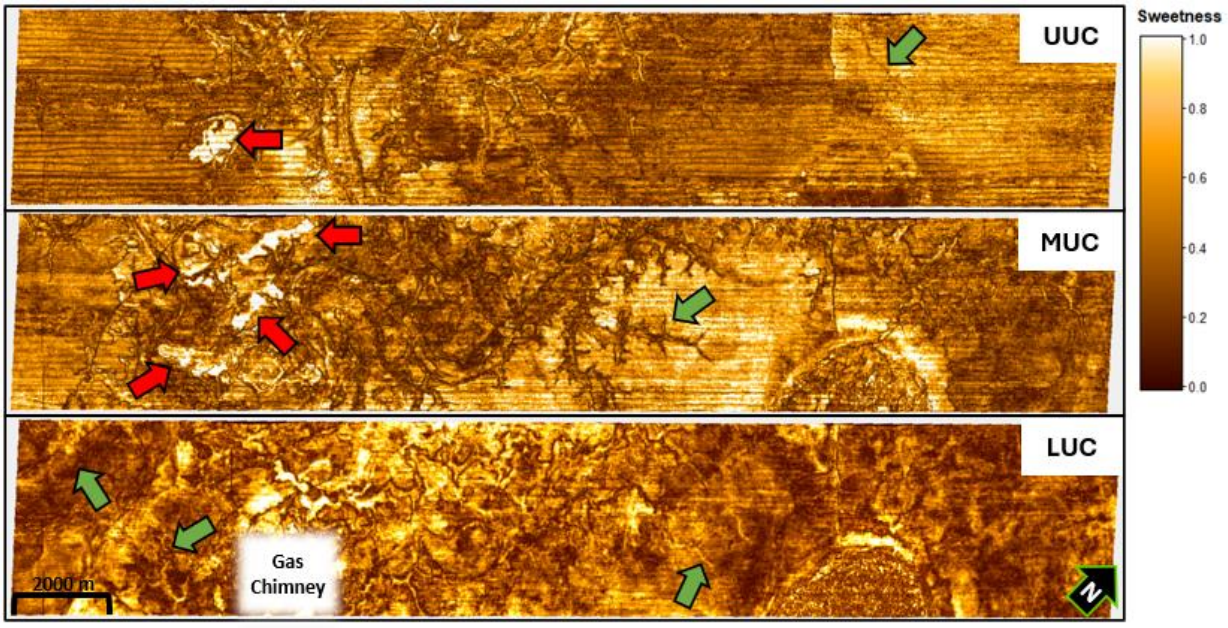

Figure 11: Sweetness attribute extracted along each unconformity. The attribute permits further visualization of subtle channels and highlights sands (high values) and shales (low values). The green arrows indicate subtle channels which were revealed by sweetness, and the red arrows indicate abnormally high sweetness anomalies. The northeast-southwest trending acquisition footprint becomes more prominent with decreasing depth.

Sobel Filter

As stated previously, Sobel filter increased the visibility of the acquisition footprint, however, the strengths of the attribute easily outweighed its constraints. To elaborate, through the detection of abrupt changes in seismic waveforms, Sobel filter significantly enhanced channel and tributary margins along each unconformity. These enhancements are indicated by green arrows in Figure

12. In addition to enhancing fluvial features, the attribute revealed structural elements throughout the HR3D volume which were previously overlooked. More specifically, along the LUC where the structural framework is more complex, Sobel filter detected and highlighted several subtle, north-south oriented, normal faults located directly adjacent to the gas chimney. These faults, indicated by yellow arrows in Figure 12, exhibit minor vertical offset and were therefore obscured in the original HR3D volume.

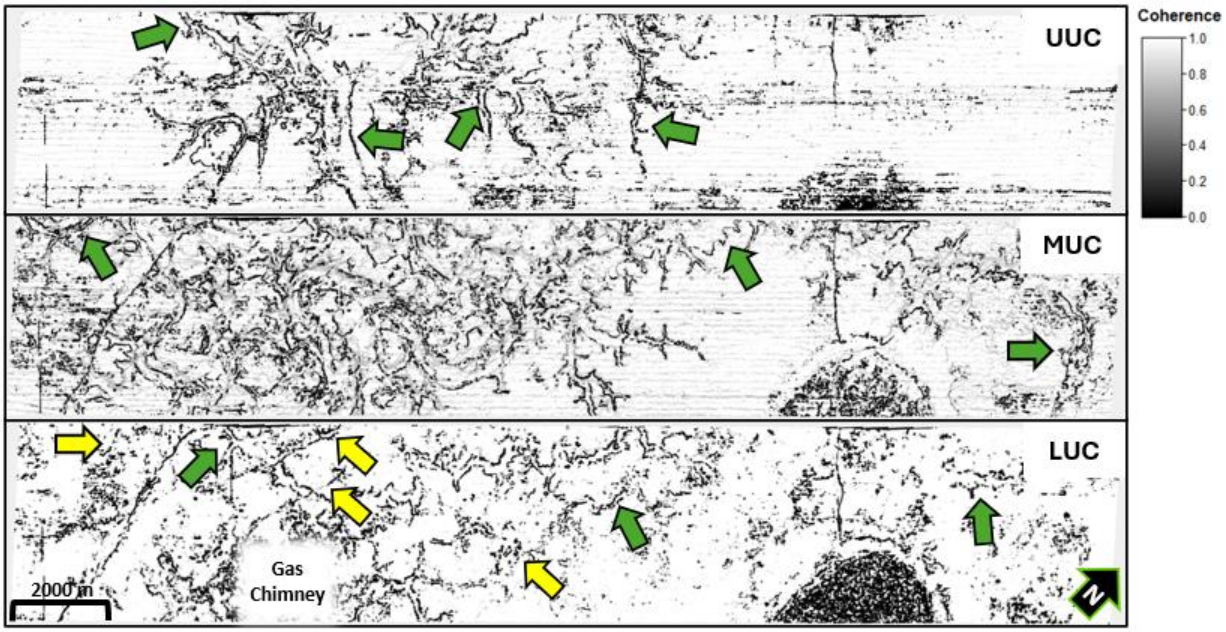

Figure 12: Sobel filter attribute extracted along each unconformity. The attribute highlights sudden changes in the seismic waveforms such as those encountered at channel margins and along faults. The green arrows indicate channel or tributary margins which have been enhanced, and the yellow arrows indicate subtle, previously overlooked faults which can now be detected. The northeast-southwest trending acquisition footprint becomes more prominent with decreasing depth.

Most-Positive (K_1) Curvature and Most-Negative (K_2) Curvature

Like Sobel filter, k_1 and k_2 curvature also enhanced the visibility of the acquisition footprint. Although the effects were worse than those of Sobel filter, the strengths of the curvature attributes still outweighed their constraints—especially when corendered with Sobel filter. Because they are inherently characterized by concave seismic reflectors, most-negative curvature effectively

detected and highlighted channel thalwegs along each unconformity. Seismic reflectors often display their most-negative curvatures in the maximum depth of each channel which contributed to the emphasis on the thalwegs as indicated by blue arrows in Figure 13. The computation of most-negative curvature confirmed that channel thalwegs are well-preserved along each unconformity. Moreover, they are especially well-preserved along the MUC. In addition to highlighting channel thalwegs, k_2 curvature also highlighted the hanging walls of normal faults as the attribute is highly sensitive to the concave deformation of the hanging wall sediments. Due to the greater structural deformation with increased depth, these concave sediments are best observed adjacent to normal faults along the MUC and LUC as indicated by green arrows in Figure 13.

Levees, which form along channel margins by the deposition of coarse-grained sediments during flooding events, are present throughout much of the HR3D volume. Because they are inherently characterized by convex seismic reflectors, most-positive curvature detected and highlighted several levee deposits. The computation of most-positive curvature revealed that the presence of levees is not ubiquitous across all channels. Rather, it unveiled that levee development is primarily associated with the most robust channels such as those along the MUC. These deposits are indicated by red arrows in Figure 13. Opposite of k_2 curvature, k_1 curvature highlighted the foot walls of normal faults as the attribute is highly sensitive to the convex deformation of the foot wall sediments. Once again, due to the greater structural deformation with increased depth, these convex sediments are best observed adjacent to normal faults along the LUC as indicated by yellow arrows in Figure 13.

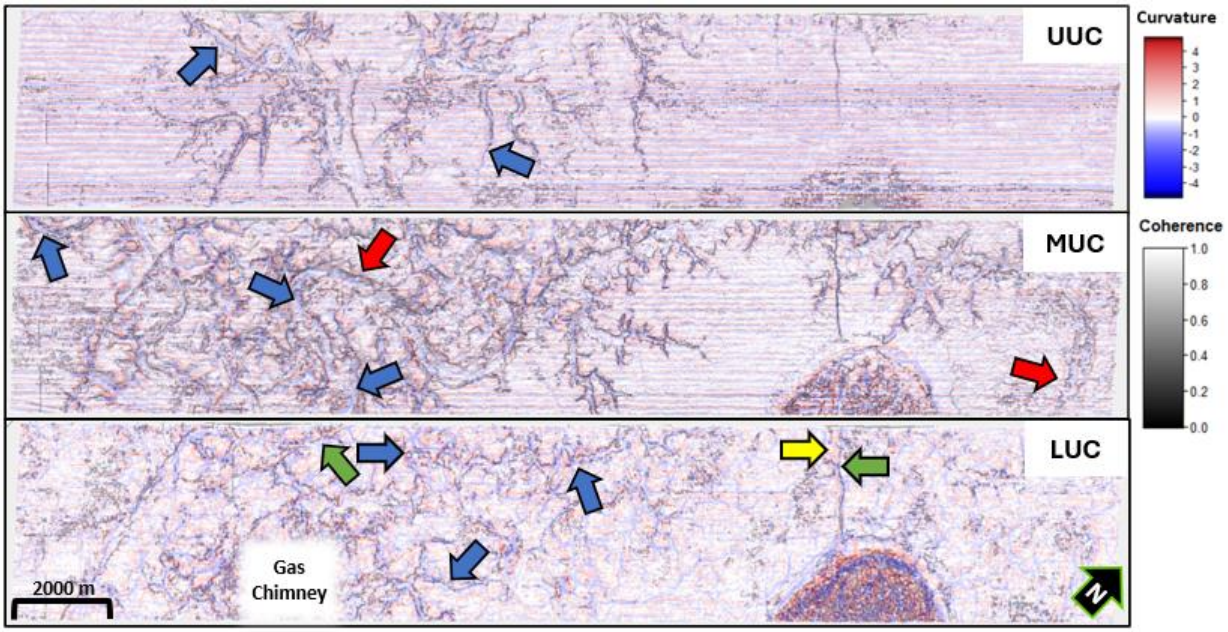

Figure 13: Corendered k_1 and k_2 curvature and Sobel filter along each unconformity. K_1 curvature highlights convex seismic reflectors (levees and foot walls of normal faults), and k_2 curvature highlights concave seismic reflectors (channel thalwegs and hanging walls of normal faults). The red and yellow arrows indicate levees and normal fault foot walls, respectively. The blue and green arrows indicate channel thalwegs and normal fault hanging walls, respectively. The northeast-southwest trending acquisition footprint becomes more prominent with decreasing depth.

Valley Shape

Because valley shape is derived from k_1 and k_2 curvature, it also enhanced the visibility of the acquisition footprint. However, the strengths of the valley shape attribute still outweighed its constraints—especially when corendered with Sobel filter. To elaborate, through the detection of "valley-shaped" seismic reflectors, the attribute effectively enhanced channel and tributary bases along each unconformity as indicated by green arrows in Figure 14. Additionally, valley shape revealed significant scours at sharp turns of the main meandering channel along the MUC. These scours are indicated by yellow arrows in Figure 14.

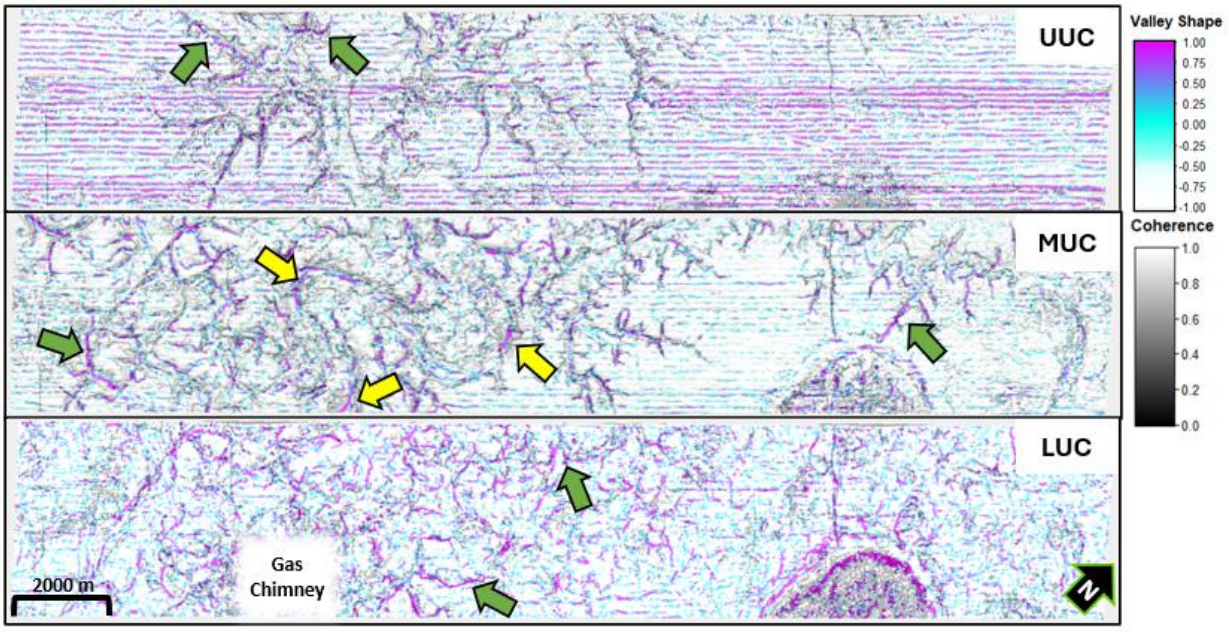

Figure 14: Corendered valley shape and Sobel filter along each unconformity. The attribute highlights seismic reflectors which are valley-shaped (i.e., channels and scours). The green arrows indicate channel or tributary thalwegs which have been enhanced, and the yellow arrows indicate erosive scours. The northeast-southwest trending acquisition footprint becomes more prominent with decreasing depth.

Clearly, seismic attributes played a crucial role in revealing key insights into fluvial features and structural elements along each unconformity. By computing a diverse array of attributes, different aspects of the unconformities and their geologic features were able to be analyzed. The knowledge gained from these attributes was later used to confirm that the channels along each unconformity satisfy the criteria of incised valleys which facilitated an understanding of eustatic sea level and constrained the proposed sequence stratigraphic model. Seismic attributes also permitted the evaluation of channel evolution in response to sea level fluctuations and were used as input in a PCA in an attempt to elucidate lithologic distribution throughout the HR3D survey.

Machine Learning: Principal Component Analysis (PCA)

The employment of spectrally balanced amplitude, sweetness, valley shape, peak frequency, and peak magnitude in a PCA yielded highly favorable results. Interestingly, regardless of valley

shape's impact on the acquisition footprint, said combination of attributes did not significantly enhance its visibility. Instead, the algorithm appeared to preferentially depict the input attributes' strengths over their weaknesses, thereby yielding a complementarity among all input attributes. More specifically, spectrally balanced amplitude and sweetness work together to highlight both the major and subtle fluvial features across the volume while valley shape enhances channel and tributary thalwegs and scours. Meanwhile, peak frequency and peak magnitude help to highlight variations in lithologic properties across various fluvial features and architectural elements throughout the HR3D volume. As depicted in Figure 15, certain colors appear to correspond with certain architectural elements along each unconformity and may thereby infer lithologic distribution.

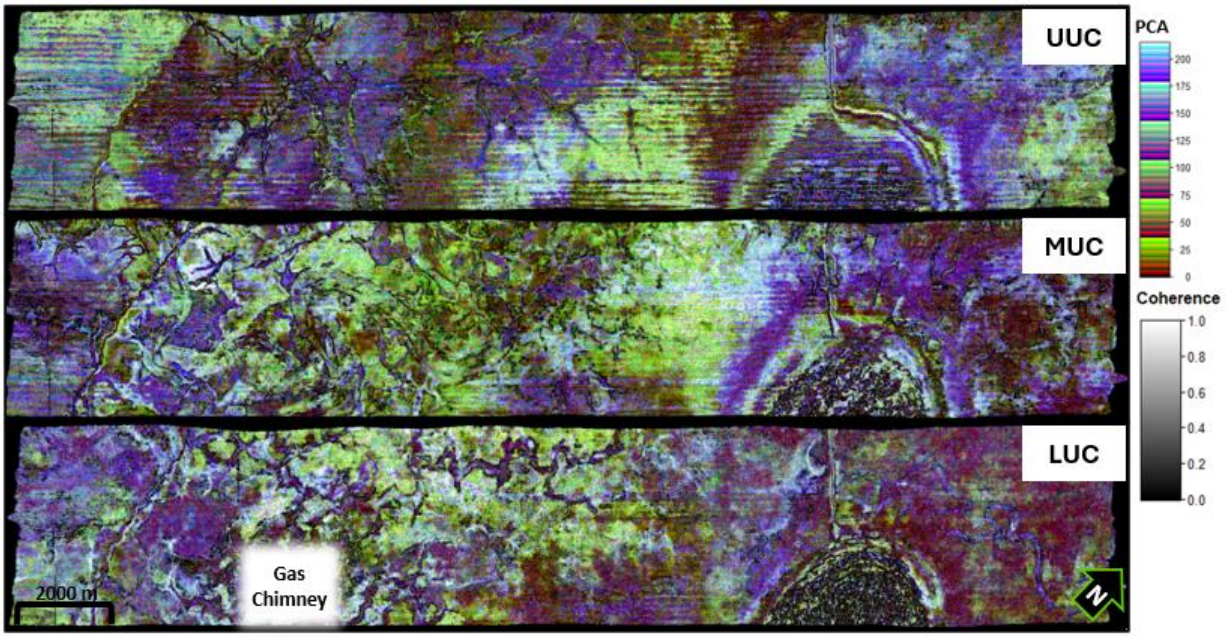

Figure 15: Corendered PCA (spectrally balanced amplitude, sweetness, valley shape, peak frequency, and peak magnitude) and Sobel filter extracted along each unconformity.

DISCUSSION

Overview of HR3D Fluvial Features

The comprehensive attribute analysis revealed complex and robust fluvial systems along the LUC, MUC, and UUC. Due to the study area's proximity to the present-day Brazos River Delta, the channels along each unconformity are most likely related to the Brazos River. This idea is in concurrence with Abdulah et al. (2004) who used 3,400 km of 2D seismic data and biostratigraphic data to map paleolocations of the Brazos Incised Valley System and Brazos River Delta over the past 200,000 years. Further, their findings suggest that the Brazos River previously avulsed eastward of its current location and was thereby more proximal to the HR3D survey throughout much of the Pleistocene.

Although most of the channels are likely related to the Brazos River, it remains possible that the Trinity River also contributed to the development of the study area. Anderson et al. (2004) used 25,000 km of high-resolution 2D seismic data and biostratigraphic data to map the Trinity Incised Valley System from the previous 140,000 years. Their findings suggest that the system lies only a short distance east-northeast of the study area, deeming it plausible that some of the channels throughout the HR3D volume originated from the Trinity River. Given the restricted extent—29 km^2—of the HR3D survey, definitive attribution of the channels to either the Brazos or Trinity fluvial systems cannot be made. However, this limitation does not hinder the study as a basic understanding of channel morphology and flow direction is of greater importance. Because the fluvial features along each unconformity trend north to south, their paleo flow is interpreted to be in the southern direction. Importantly, this idea is supported by confluence angles between tributaries and main channels along each unconformity.

Interaction Between Low Gradient Shelf and Frequent Sea Level Changes

Currently, the study area exists in shallow water depths of 14 to 15 meters on the GoM's gently sloped shelf which displays an average gradient of only 0.3 meters per 2.4 kilometers (Geyer et al., 2024). Throughout much of the Quaternary, this subtle gradient has significantly impacted coastal fluvial systems, such as the Brazos and Trinity Rivers, as minor fluctuations in vertical base level have caused significant horizontal variations in shoreline position. These disproportionate variations have facilitated rapid updip migration of knick points during forced regressions and rapid updip flooding amidst transgressions. Additionally, because global sea level has frequently fluctuated by more than 130 meters over the past 400,000 years, the study area has been subject to everchanging depositional environments (Johnson and Watt, 2012). These factors permit the application of sequence stratigraphic techniques throughout the interval of interest given the presence of well-preserved depositional sequences and their associated systems tracts.

Importance of Unconformities and Incised Valleys in Sequence Stratigraphy

In seismic stratigraphic analyses, unconformities act as sequence boundaries as they mark the beginning of a new sea level cycle (Mitchum et al., 1977). Therefore, unconformities serve as the fundamental framework for constructing a stratigraphic model. Because they form by subaerial exposure and subsequent erosion of the continental shelf, unconformities often host incised valleys which form by the response of fluvial systems to drastic reductions in base level. To be classified as an incised valley, a fluvial channel must satisfy the criteria set forth by Dalrymple et al. (1994) and Posamentier (2001). Moreover, the valley must be a) regionally extensive, b) larger than a single channel, and c) accompanied by tributary valleys which feed the main valley. Postamentier (2001) also maintains that incised valleys on gently sloped shelves—like that of the GoM—often demonstrate a dendritic geometry. Because the channels along the UUC, MUC, and LUC meet

these requirements and demonstrate dendritic geometries, they can confidently be referred to as incised valleys, and it can be inferred that each of the mapped unconformities formed because of low sea level. Thus, each unconformity should correspond to a period of substantially decreased eustatic sea level on the curve from Johnson and Watt (2012). Because the UUC, MUC, and LUC lie at extremely shallow depths within the HR3D volume, recent glacial maximums (i.e., significant eustatic lowstand stages) such as marine isotope stages (MIS) 2, 6, and 8 are likely responsible for their existence. The relatively insignificant decrease in sea level during the MIS4 lowstand deems its contribution to the development of a seismically detectable unconformity across the study area unlikely. Therefore, neither the UUC, MUC, or LUC are believed to have formed during the MIS4 lowstand. Due to the absence of well and biostratigraphic data throughout the interval of interest, previous nearby studies of the shallowest subsurface were relied upon to approximate the age of each unconformity.

Correlating the Upper Unconformity to a Eustatic Lowstand Event

Because the UUC is the shallowest unconformity within the HR3D volume at a depth of only 17 meters below the sea floor, it would be most logical that this unconformity formed during the last glacial maximum 30 to 17 ka. Due to the abundance of published literature concerning the shallowest subsurface throughout the northern GoM, this hypothesis was easily investigated. Simms et al. (2007) used a combination of 20,000 km of high-resolution 2D seismic data, oxygen isotopic data, and biostratigraphic data from the northwestern GoM to regionally map the unconformity which corresponds to the last glacial maximum—the MIS2 Unconformity. Moreover, their detailed analysis revealed that the MIS2 unconformity lies at depths ranging from 10 to 140 mbsf. According to their regional contour map, the unconformity lies at its greatest depth of 140 mbsf farthest offshore from the present-day coastline of Texas. Conversely, the

unconformity lies at depths as shallow as 10 mbsf proximal to the present-day coastline of Texas. When the boundary of the HR3D survey is georeferenced on Simms et al. (2007)'s contour map, the MIS2 unconformity lies at an approximate depth of 16 mbsf across the HR3D area. This depth closely matches the calculated depth of 17 mbsf at which the UUC lies throughout the HR3D volume.

In another study, Anderson et al. (2016) relied upon similar data—2D seismic data, oxygen isotopic data, and biostratigraphic data—to generate a regional digital elevation model (DEM) of the MIS2 unconformity throughout the northwestern GoM. In concurrence with the contour map of Simms et al. (2007), Anderson et al. (2016)'s DEM verified that the MIS2 unconformity lies at shallow depths and greater depths proximal and distal to the present-day coastline of Texas, respectively. When the boundary of the HR3D survey is georeferenced on Anderson et al. (2016)'s DEM, the MIS2 unconformity lies at an approximate depth of 20 mbsf across the HR3D area which, once again, closely matches the calculated depth of 17 mbsf at which the UUC lies throughout the HR3D volume. Given that two previous studies have estimated the MIS2 unconformity to exist at depths of 16 and 20 mbsf across the HR3D survey, it can be asserted with considerable certainty that the UUC—at a depth of 17 mbsf—is correlative to the MIS2 unconformity.

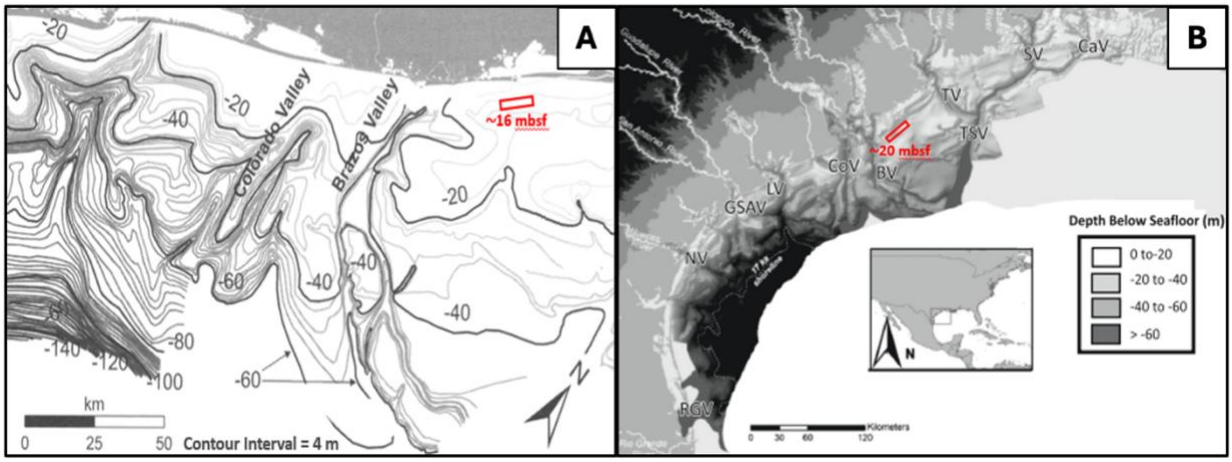

Figure 16: A) Modified from Simms et al. (2007). A regional contour map of the MIS2 unconformity in the northwestern GoM. The red rectangle represents the HR3D boundary, and the MIS2 unconformity lies at 16 mbsf across the survey. B) Modified from Anderson et al. (2016). A regional digital elevation model of the MIS2 unconformity in the northwestern GoM. The red rectangle represents the HR3D boundary, and the MIS2 unconformity lies at 20 mbsf across the survey. These depths closely correspond to the depth of the UUC which lies at 17 mbsf across the HR3D survey. Therefore, the UUC is likely equivalent to the MIS2 unconformity.

Correlating the Middle Unconformity to a Eustatic Lowstand Event

Because the MUC is the next major unconformity at a depth of 60 mbsf, it would be most logical that it formed during the MIS6—the glacial maximum which preceded the MIS2—approximately 190 to 130 ka. Once again, the abundance of published literature concerning the shallowest subsurface throughout the northern GoM allowed for this hypothesis to be investigated. Although the studies by Simms et al. (2007) and Anderson et al. (2016) thoroughly explored the MIS2 unconformity, older stratigraphic features such as the MIS6 unconformity were not investigated. However, Anderson et al. (1992) used a combination of 2,700 km of high-resolution 2D seismic data, oxygen isotopic data, and biostratigraphic data to conduct a more comprehensive study of the shallow stratigraphy in the northwestern GoM which included the MIS6 unconformity. The results of the study suggest that in Galveston Bay—40 km to the northeast of the study area—the MIS6 unconformity lies at an approximate depth of 54 mbsf. This depth was calculated at an

interval velocity of 1,550 m/s. At Exxon's interval velocity of 1,525 m/s, this translates to a depth of 53 mbsf, which still closely corresponds to the subsurface depth of 60 mbsf at which the MUC lies across the HR3D area. Additionally, within the same seismic line, Anderson et al. (1992) also estimated the MIS2 unconformity to lie 11 mbsf at an interval velocity of 1,550 m/s. At such shallow depths, minor differences in velocity—1,550 m/s versus 1,525 m/s—produce negligible changes in depth. Therefore, the MIS2 unconformity remains at an approximate depth of 11 mbsf with Exxon's interval velocity of 1,525 m/s. These findings reinforce the idea that the UUC is correlative to the MIS2 unconformity and strongly suggest that the MUC is correlative to the MIS6 unconformity. While Anderson et al. (1992) found the MIS2 and MIS6 unconformities to lie at slightly shallower depths in Galveston Bay than the UUC and MUC in the HR3D survey, this discrepancy can be explained by the fact that their study was conducted many kilometers updip from the HR3D study area—especially since both unconformities lie at reduced depths.

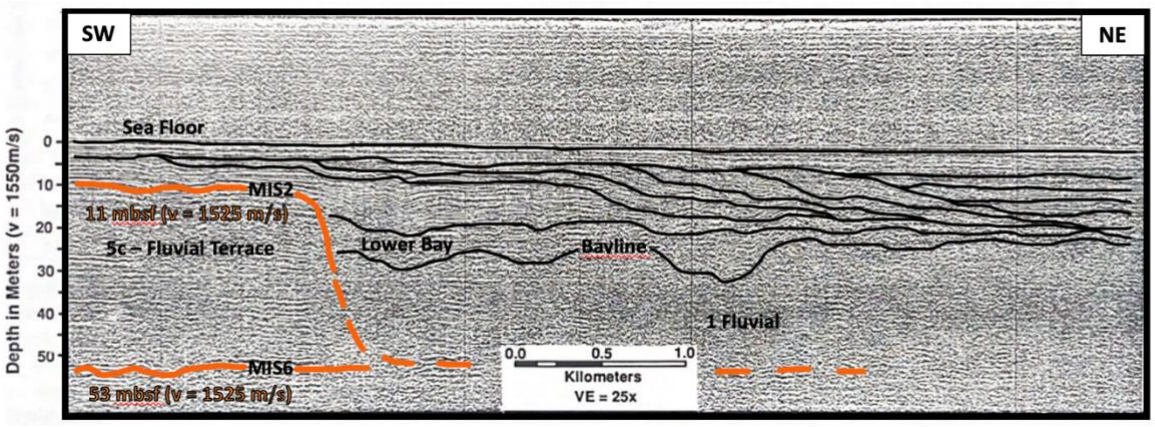

Figure 17: Modified from Anderson et al. (1992). An interpreted seismic line from Galveston Bay (40 km northeast of the study area). The MIS2 and MIS6 unconformities are interpreted to lie at 11 mbsf and 53 mbsf, respectively. The depth of the MIS6 unconformity closely corresponds to the depth of the MUC which lies at 60 mbsf across the HR3D survey. Therefore, the MUC is likely equivalent to the MIS6 unconformity.

Correlating the Lower Unconformity to a Eustatic Lowstand Event

Because the LUC is the next major unconformity at a depth of 112 mbsf, it would be most logical that it formed during the MIS8—the glacial maximum which preceded the MIS6—approximately 280 to 250 ka. Unfortunately, unlike the MIS2 and MIS6 unconformities, the MIS8 unconformity is not well-documented in the GoM. Therefore, no published literature is available to confirm or deny this preconceived notion. Rather, knowledge of eustatic sea level events and sequence stratigraphy were relied upon to further investigate the idea that the LUC is correlative to the MIS8 unconformity.

HR3D Sequence Stratigraphy

Mitchum et al. (1977) define a depositional sequence as a "stratigraphic unit composed of a relatively conformable succession of genetically related strata which is bounded at its top and base by unconformities or their correlative conformities." With high confidence that the UUC and MUC formed during the MIS2 and MIS6 lowstands and reason to believe that the LUC formed during the MIS8 lowstand, these unconformities (i.e., sequence boundaries) serve as the framework of the stratigraphic model and provide constraint when relating the model to past sea level and geologic time. Through the use of a tripartite scheme like that applied by Pigott et al. (2011) in the Gulf of Thailand, each depositional sequence was subdivided into three parts—LST, TST, and HST.

Typically, seismic stratigraphic analyses utilize large, conventional 3D seismic surveys which may span from 1,000 to more than 10,000 km^2. Additionally, such analyses are often conducted along depositional dip and therefore require the survey to be laterally extensive in the basinward direction. These factors permit the regional evaluation of clinoforms and seismic reflector configuration which is utilized to define and classify depositional systems tracts as LSTs, TSTs, and HSTs are commonly characterized by progradational, retrogradational, and aggradational to

progradational reflectors, respectively (Catuneanu et al., 2011). Because the HR3D survey spans less than 30 km^2 and only extends approximately 2.5 km in the basinward direction, the classification of systems tracts based upon seismic reflector configuration was unsuitable for this study. Thus, a more subjective approach which involved the identification of transgressive surfaces and maximum flooding surfaces was taken in distinguishing the LSTs, TSTs, and HSTs from one another.

Seismically, a transgressive surface is a laterally continuous reflector which represents the time at which accommodation exceeded sediment supply (Cattaneo and Steel, 2003). On the continental shelf, transgressive surfaces commonly extend over incised valleys and thereby separate overlying transgressive deposits from underlying lowstand deposits (Weimer, 1992). Using this logic, within each sequence, the laterally continuous seismic reflector which immediately overlies the incisions along each unconformity was classified as a transgressive surface. Because a transgressive surface defines the lowermost limit of the TST, it also defines the uppermost limit of the LST. Therefore, the identification of transgressive surfaces resulted in the complete definition of LSTs within each sequence—bounded by an unconformity at their base and a transgressive surface at their top.

Within each sequence, LSTs onlap the underlying unconformity and are confined to valley incisions. Moreover, the LSTs associated with the MUC and UUC exhibit greater thicknesses than the LST associated with the LUC. This is owed to the superior incision depths of 42 and 43 meters along the MUC and UUC in comparison to the incision depth of 33 meters along the LUC. Such differences in the depth of maximum incision along each unconformity can be explained by the difference in magnitude of sea level fall. According to Johnson and Watt (2012)'s sea level curve, during the MIS6 and MIS2 lowstands, when the MUC and UUC formed, sea level decreased by

125 and 130 meters, respectively. However, during the MIS8 lowstand, when the LUC formed, sea level decreased by only 100 meters.

During the subsequent periods of rapid transgression, valley-fill within each sequence was likely influenced and manipulated by estuarine processes. Valley-fill is not uniform across each LST as a portion of the main channel along the MUC exhibits clear internal amalgamation. Conversely, the remainder of the main channel along the MUC and the main channels along the LUC and UUC exhibit only undifferentiated fill. These differences imply that either a more complex interplay of autogenic and allogenic factors such as sea level, subsidence, climate, and sediment supply existed during MUC's LST's time of deposition or that such features were simply not preserved within the LUC's and UUC's LSTs (Saha and Bhattacharya, 2023). Nonetheless, based upon the comprehensive attribute and machine learning analysis, the lowstand fill of each valley system is believed to predominantly consist of fine-grained fluvial and estuarine sediments.

Seismically, a maximum flooding surface is a laterally continuous reflector which represents the time at which sea level reached its maximum. Moreover, these surfaces are commonly composed of fine-grained sediments and mark the transition from fining-upward to coarsening-upward deposition (Van Wagoner, 1995). Thus, within each sequence, the first laterally continuous, positive seismic reflector up-section from the transgressive surface was classified as a maximum flooding surface. Because a maximum flooding surface defines the lowermost limit of the HST, it also defines the uppermost limit of the TST. Therefore, the identification of maximum flooding surfaces resulted in the complete definition of TSTs and HSTs within each sequence with TSTs being bounded by a transgressive surface at their base and a maximum flooding surface at their top and HSTs being bounded by a marine flooding surface at their base and an unconformity at

their top. This culminated the complete tripartite seismic stratigraphic interpretation within the shallowest 200 milliseconds of the HR3D volume.

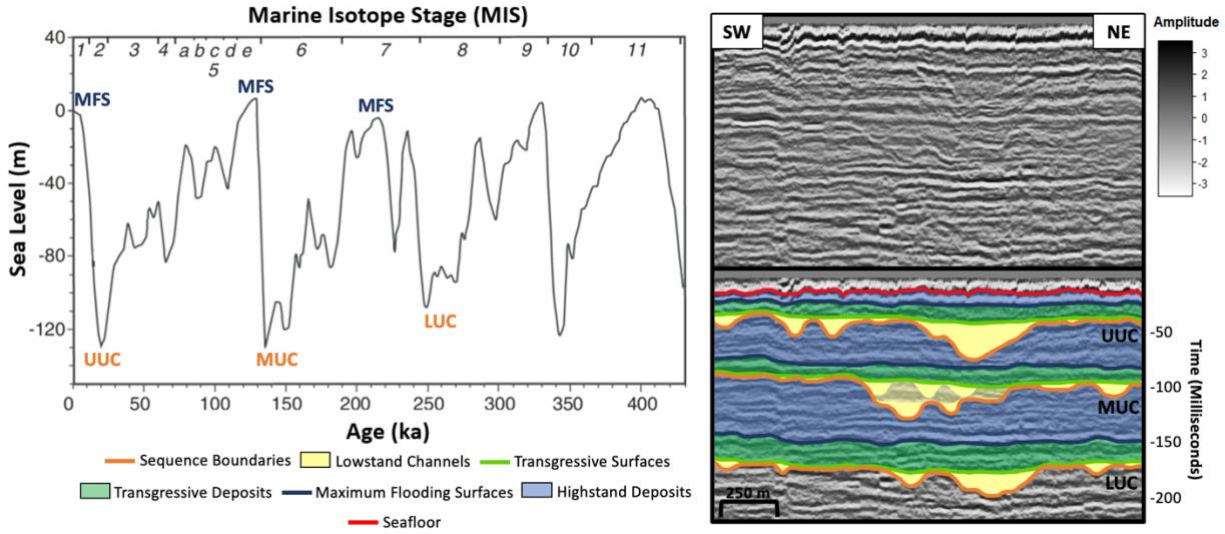

Figure 18: Seismic inline 195 showing the complete tripartite (LST, TST, and HST) interpretation of the defined sequences. The LUC, MUC, and UUC are correlated to lowstand events, and MFSs are correlated to highstand events on Johnson and Watt (2012)'s sea level curve.

Orders of Sea Level Cyclicity and Hierarchy

As previously discussed, the sediments which comprise a depositional sequence were deposited during the various phases of a sea level cycle. Since the late 1970s, it has been well-established that five orders—first-order, second-order, third-order, fourth-order, and fifth-order—of sea level cyclicity exist based upon the amplitude of sea level change, duration, and sea level rise and fall rates (Vail et al., 1977b; Mitchum et al., 1990; Goldhammer et al., 1991). Moreover, first-order cycles are characterized by slow sea level rise and fall rates—less than 1 centimeter/1,000 years—and occur over a significant length of geologic time—200 to 400 million years. On the opposite end of the spectrum, fifth-order cycles are characterized by rapid sea level rise and fall rates—60 to 700 centimeters/1,000 years—and occur over an insignificant length of geologic time—0.01 to 0.2 million years (Goldhammer et al., 1990; Vail et al., 1977). Clearly, a considerable amount of

variability exists between the orders of sea level cyclicity. Therefore, as with any sequence or seismic stratigraphic study, it is important to understand the order of sea level cyclicity in which the sequences of interest were deposited. Thus, to determine their order, the defined sequences were assessed according to the criteria set forth by Vail et al. (1977), Mitchum et al. (1990), and Goldhammer et al. (1990) as shown in Table 4.

Cycle Order	Thickness Range (m)	Sea Level Amplitude (m)	Duration (ma)	Sea Level Rise/Fall Rate (cm/1,000 yr.)	Cause
First	300 – 3,000	> 100	200 - 400	< 1	Formation and breakup of supercontinents
Second	150 – 1,500	50 – 100	10 – 100	1 – 3	Volume changes in global mid-oceanic ridge systems
Third	150 - 450	50 – 100	1 – 10	1 – 10	Problematic; mid-oceanic ridge changes, continental ice growth/decay, etc.
Fourth	6 - 150	1 – 150	0.2 – 0.5	40 – 500	Milankovitch glacioeustatic cycles
Fifth	3 - 60	1 – 150	0.01 – 0.2	60 – 700	Milankovitch glacioeustatic cycles

Table 4: Summarized from Vail et al. (1977), Mitchum et al. (1990), and Goldhammer et al. (1990). Sea level cycle order hierarchy and their typical sequence thickness, sea level amplitude, duration, sea level rise and fall rates, and cause.

The approximate thicknesses of the lowermost and middle sequences were estimated to be 52 and 43 meters, respectively. Additionally, the approximate thickness of the uppermost sequence was estimated to be 17 meters, however, its thickness was not taken into consideration being that the sequence remains incomplete. According to Johnson and Watt (2012)'s sea level curve, the amplitude of sea level change over which the lowermost, middle, and uppermost sequences were deposited was 105, 138, and 130 meters, respectively. Further, the duration of time over which the lowermost and middle sequences were deposited was 112 ka and 116 ka, respectively. For the same reason as before, the duration of the uppermost sequence could not be taken into consideration. From Johnson and Watt (2012)'s sea level curve, the lowermost sequence's rate of sea level rise was estimated to be 318 centimeters/ 1,000 years, and the rate of sea level fall was estimated to be 158 centimeters/ 1,000 years. The middle sequence's rate of sea level rise was

estimated to be 1,971 centimeters/ 1,000 years, and the rate of sea level fall was estimated to be 127 centimeters/ 1,000 years. Finally, the uppermost sequence's rate of sea level rise was estimated to be 650 centimeters/ 1,000 year. Once again, because the uppermost sequence is incomplete, its rate of sea level fall could not be taken into consideration.

The assessment of each depositional sequence's thickness, amplitude of sea level change, duration, and sea level rise and fall rates suggests that each sequence was deposited within a fifth-order sea level cycle and can therefore be referred to as fifth-order sequences. Moreover, such sea level cycles are believed to be controlled by glacioeustasy which is in strong concurrence with the known cause of Late Quaternary sea level fluctuations (Vail et al., 1977; Pigott et al., 2011).

Fifth-Order Implications for Hydrocarbon Reservoirs

Globally, economically viable hydrocarbon exploration and development is focused upon reservoirs which were deposited within second, third, and sometimes fourth-order sea level cycles. Van Wagoner (1995) states that fourth-order sequences are the building blocks of most reservoirs. This is where the hierarchy and superimposition of sea level cycles and their depositional sequences become of significant importance. Moreover, as shown in Figure 19, a second-order sequence is comprised of many third, fourth, and fifth-order sequences; a third-order sequence is comprised of fourth and fifth-order sequences, and a fourth-order sequence is comprised of fifth-order sequences. Therefore, if fourth-order sequences are the building blocks of reservoirs and are comprised of fifth-order sequences, fifth-order sequences directly contribute to reservoir heterogeneity. As previously discussed, the intricacies of fifth-order sequences are below the resolution of conventional seismic methods. Thus, in areas with limited well control, enhanced knowledge of these sequences and their vertical and lateral distribution through high-resolution methods may provide insight into small-scale reservoir heterogeneity. Additionally, Van Wagoner

et al. (1990) maintain that fifth-order sea level cycles impact the location of stratigraphic traps. Therefore, the significance of fifth-order sea level cycles lies not only in their influence on small-scale reservoir heterogeneity but also in the positioning of traps. Such factors deem an understanding of these high-frequency sea level fluctuations and their associated sequences as vital in the exploration and development of hydrocarbon fields.

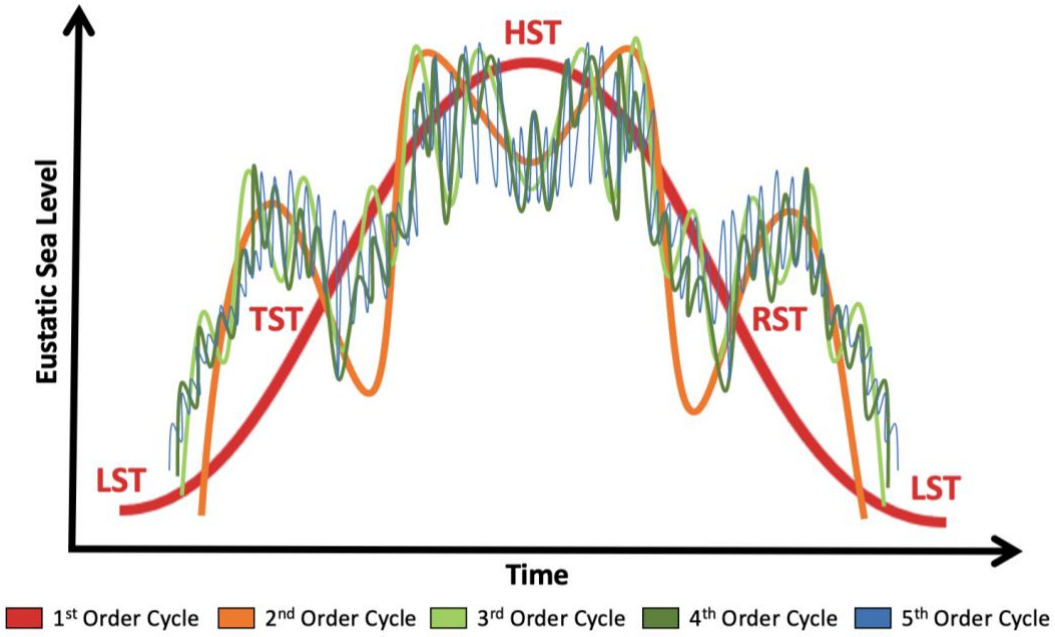

Figure 19: Conceptual relationship between time and sea level cyclicity. Within one first-order cycle (LST, TST, HST, RST, LST), several second-order cycles will occur. Within one second-order cycle, several third-order cycles will occur. Within one third-order cycle, several fourth-order cycles will occur. Within one fourth-order cycle, several fifth-order cycles will occur. Axes are unitless as the figure is only meant to demonstrate the hierarchy and superimposition of sea level cycle orders.

Valley Evolution

Undoubtedly, the incised valleys within each sequence underwent some form of evolution in response to fluctuating sea level. These changes were best preserved along the MUC and were easily evaluated within the flattened, spectrally balanced amplitude volume. Furthermore, it was determined that the system was originally a simple meandering channel devoid of dendritic

characteristics. As time progressed, the channel nearly tripled in width as it grew from an initial width of 100 meters to a final width of 280 meters. The channel also became increasingly sinuous as it went from an initial sinuosity of 2.7 to a final sinuosity of 2.8. Further, the channel developed robust chute channels and a complex network of dendritic crevasse splays and tributaries which appear to be well-developed at a time of approximately 100 milliseconds as demonstrated in Figure 20. These dendritic crevasse splays and tributaries expanded to their maximum dimensions and spatial extent, as depicted in Figure 20, before ultimately becoming buried by more recent sediments.

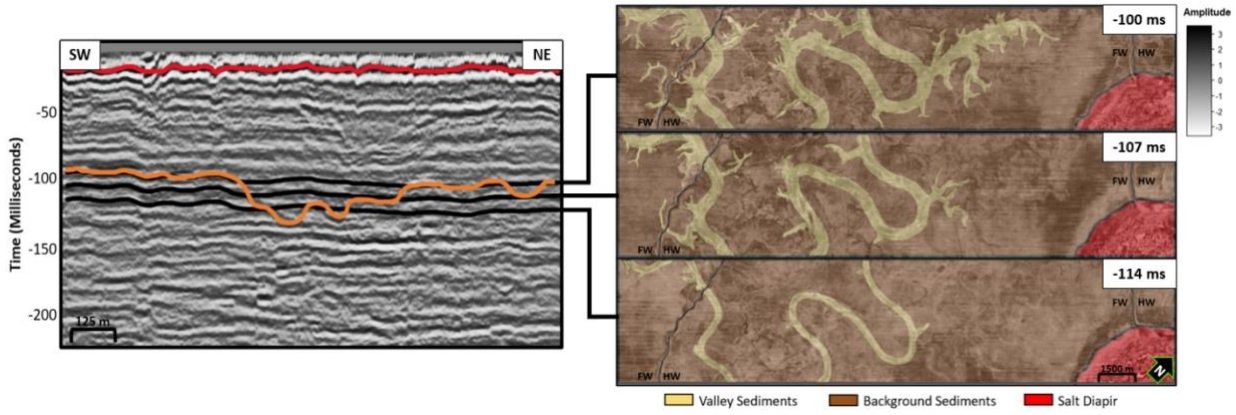

Figure 20: Interpreted horizon slices from the spectrally balanced amplitude volume flattened upon the reference horizon. Horizon slices show valley evolution from 114 to 100 milliseconds. The system begins as a simple meandering channel devoid of dendritic characteristics. Moving shallower, the channel becomes increasingly wide and sinuous and develops a network of dendritic crevasse splays and tributaries. The foot walls and hanging walls of the two major faults are also labeled as indicated by FW and HW, respectively.

Valley Evolution in Response to Transgression

Various studies have thoroughly investigated Quaternary sea level fluctuations and the subsequent evolution of fluvial systems on the inner shelf of the Gulf of Thailand (Pigott et al., 2011; Reijenstein et al., 2011). Like this study, these analyses focused upon stratigraphic sequences associated with the high-frequency, Quaternary sea level cycles and include channels which exhibit closely similar geomorphology to those within the HR3D volume. Moreover, many of the

channels in the shallowest subsurface of the Gulf of Thailand also originate as simple meandering channels which become increasingly dendritic with time. Pigott et al. (2011) determined that this drastic change in channel morphology occurs when a major lowstand event is immediately followed by rapid transgression. According to Johnson and Watt (2012)'s sea level curve, this trend was prominent during the defined sequences' time of deposition.

To elaborate, when sea level begins to fall, initial channel progradation onto the shelf occurs as fluvial systems respond to a reduction in base level. During the lowstand phase, the shelf reaches its maximum subaerial exposure which leads to the significant and robust incision of valleys across the shelf. These channels exhibit fluvial-dominated, basinward—in this case, southern—flow until sea level begins to rise again. This initial increase in base level often forces the channels to become more sinuous (Scamardo and Kim, 2016). As sea level continues to rise and accommodation exceeds sediment input, the channels become overpowered by marine processes. Consequently, the channels become flooded beyond their original banks which facilitates an increase in channel width and the widespread development of dendritic crevasse splays and tributaries. Finally, during the highstand phase, sea level reaches its maximum, and the channels are fully drowned and buried by younger sediments. During this phase, fluvial systems are forced to remain updip within the coastal plain.

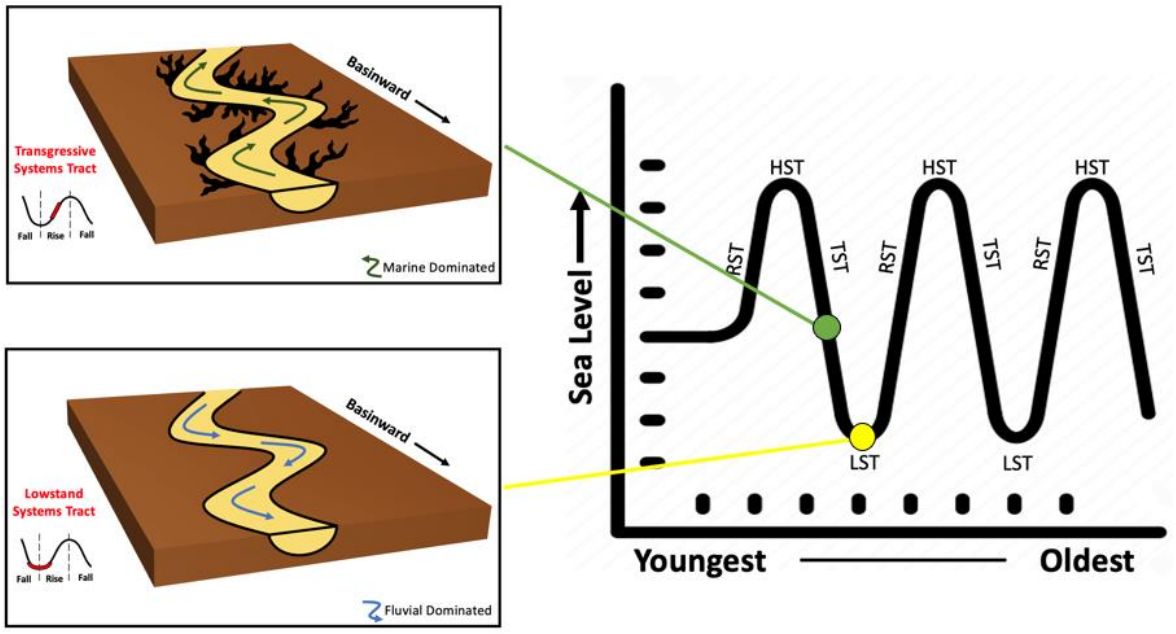

Figure 21: Demonstration of how sea level fluctuations generally influence valley morphology. During lowstand times, channels are robust as they are dominated by fluvial processes. As sea level rises, channels become flooded as they are dominated by marine processes.

Inferring Lithology from Principal Component Analysis (PCA) Results

The results of PCA were examined along each unconformity; however, they were most enlightening along the MUC due to the presence of a wide variety of architectural elements—main channels, crevasse splays, bars, and more. Basic knowledge of the general lithologic composition of these architectural elements was used to infer lithology from the PCA results. Moreover, elements which are well-known to be dominated by silts and sands such as crevasse splays and mid-channel bars are represented by purple colors across the MUC as indicated by red and pink arrows, respectively in Figure 22. Conversely, other elements which are well-known to be dominated by muds and silts such as floodplains and estuarine mud-filled channels are represented by green colors across the MUC as indicated by green and blue arrows, respectively in Figure 22.

Because no well data or core is available to confirm the relationship between coarse-grained facies and purple colors and fine-grained facies and green colors, the cross-section geometry of amplitude reflectors was investigated instead. This provided insight into the differential compaction of sediments and facilitated an enhanced understanding of lithologic composition as a "bump" is often indicative of a sand-filled element, whereas a "sag" is often indicative of a mud-filled element (Heritier et al., 1980). As anticipated, crevasse splays along the MUC exhibit a clear bump which indicates the presence of coarse-grained sediments. The main meandering channel exhibits a clear sag which indicates the presence of fine-grained sediments. Therefore, it can be confidently inferred from the PCA that purple colors correspond to coarser-grained sediments, and green colors correspond to finer-grained sediments.

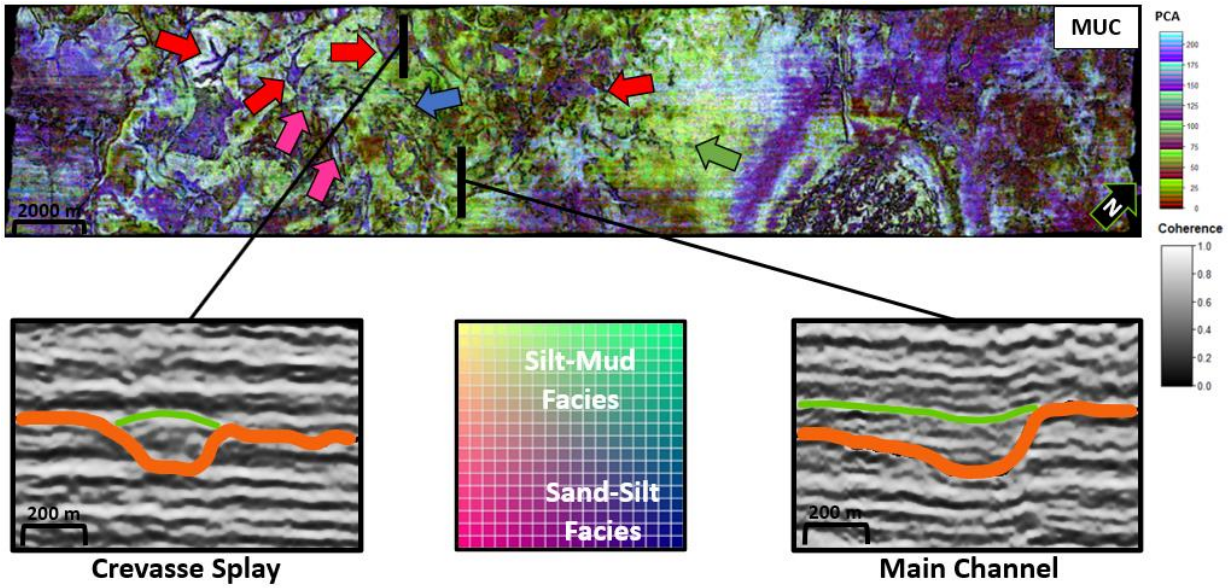

Figure 22: Corendered PCA and Sobel filter along the MUC. Facies which are typically dominated by coarse-grained sediments are represented by purple colors; red and pink arrows indicate crevasse splays and mid-channel bars, respectively. Facies which are typically dominated by fine-grained sediments are represented by green colors; green and blue arrows indicate floodplain and main channel fill, respectively. In cross-section, crevasse splays exhibit a clear bump which is indicative of sand fill, and the main channel exhibits a clear sag which is indicative of mud fill. Thus, it can be inferred that purple colors correspond to coarse-grained sediments, and green colors correspond to fine-grained sediments.

CONCLUSIONS

In conclusion, three major unconformities were identified and mapped within the shallowest 200 milliseconds of the HR3D seismic volume in the near-shore GoM. The computation of various seismic attributes was instrumental in the understanding of geologic features along each unconformity. Although many attributes were calculated, their performance was variable as some attributes—specifically geometric attributes—were hindered by the HR3D volume's strong acquisition footprint and low signal-to-noise ratio. Nonetheless, the computation of certain seismic attributes such as spectrally balanced amplitude and sweetness helped tremendously in revealing subtle fluvial features along each unconformity. Further, the channels along each unconformity were determined to be incised valleys as they satisfy the criteria set forth by previous authors. Each of the unconformities and their incised valleys formed during different glacial maximums over the past 275,000 years. Moreover, the lowstand stages during which the LUC, MUC, and UUC formed were determined to be the MIS8, MIS6, and MIS2, respectively. The depositional sequences associated with each unconformity closely suit the criteria of fifth-order sequences and were therefore deposited within fifth-order sea level cycles. These high-frequency sea level cycles are of importance as they are known to influence small-scale reservoir heterogeneity and stratigraphic trap location. In response to rapid transgression, incised valleys—specifically along the MUC—demonstrate a tendency to become increasingly sinuous and dendritic through time. Finally, the employment of spectrally balanced amplitude, sweetness, valley shape, peak frequency, and peak magnitude in a PCA provided valuable insight into lithologic distribution along the MUC. Clearly, due to limited seismic coverage and the absence of well and biostratigraphic data, interpretations of sequence stratigraphic elements—unconformities, transgressive surfaces, and maximum flooding surfaces—and lithologic distribution have their inherent limitations. However, this study

provides a general seismic stratigraphic framework for Late Quaternary deposits—which are typically unresolvable through conventional seismic methods—on the GoM's inner shelf.

REFERENCES

Al-Dossary, S., & Marfurt, K. J. (2006). Multispectral estimates of reflector curvature and rotation. Geophysics, 71, 41-51.

Anderson, J. B., Thomas, M. A., Siringin, F. P., & Smyth, W. C. (1992). Quaternary evolution of the Texas coast and shelf. In C. H. Fletcher III & J. F. Wehmiller, Quaternary Coasts of the United States: Marine and Lacustrine Systems. SEPM Special Publication, vol. 48, 253-265.

Anderson, J. B., Wallace, D. J., Simms, A. R., Rodriguez, A. B., Weight, R. W., & Taha, P. Z. (2016). The recycling of sediments between source and sink during a eustatic cycle. Earth-Science Reviews, 153, 111–138. https://doi.org/10.1016/j.earscirev.2015.10.014

Cattaneo, A., & Steel, R. J. (2003). Transgressive deposits: A review of their variability. Earth-Science Reviews, 62(3–4), 187–228. https://doi.org/10.1016/s0012-8252(02)00134-4

Catuneanu, O., Galloway, W. E., St. Clement Kendall, C. G., Miall, A. D., Posamentier, H. W., Strasser, A., & Tucker, M. E. (2011). Sequence stratigraphy: Methodology and nomenclature. Newsletters on Stratigraphy, 44(3), 173–245. https://doi.org/10.1127/0078-0421/2011/0011

Celecia, A., Figueiredo, K., Rodriguez, C., Vellasco, M., Maldonado, E., Silva, M. A., Rodrigues, A., Nascimento, R., & Ourofino, C. (2021). Unsupervised machine learning applied to seismic interpretation: Towards an unsupervised automated interpretation tool. Sensors, 21(19), 1–27. https://doi.org/10.3390/s21196347

Chopra, S., & Marfurt, K. (2016). Spectral decomposition and spectral balancing of seismic data. The Leading Edge, 35(2), 176–179. https://doi.org/10.1190/tle35020176.1

Dalrymple, R., Boyd, R., & Zaitlin, B. (1994). History of Research Types and Internal Organization of Incised-Valley Systems: Introduction to the Volume. SEPM Special Publications, 2-10.

Galloway, W. E., Whiteaker, T. L., & Ganey-Curry, P. (2011). History of Cenozoic North American drainage basin evolution, sediment yield, and accumulation in the Gulf of Mexico Basin. Geosphere, 7(4), 938–973. https://doi.org/10.1130/ges00647.1

Garcia-Reyes, A., & Dyment, J. (2022). Structure, age, and tectonic evolution of the Gulf of Mexico. Earth and Planetary Science Letters, 577, 1–8. https://doi.org/10.1016/j.epsl.2021.117259

Geyer, R. A., LaMourie, M. J., & Broadus, J. M. (2024). Gulf of Mexico. Encyclopedia Britannica. https://www.britannica.com/place/Gulf-of-Mexico

Goldhammer, R., Oswald, E., & Dunn, P. (1990). Hierarchy of stratigraphic forcing: Example from Middle Pennsylvanian shelf carbonates of the Paradox basin. Kansas Geological Survey, Bulletin 233, 361–413.

Heritier, F. E., Lossel, P., & Wathe, E. (1980). Frigg Field: Large submarine-fan trap in Lower Eocene rocks of the Viking Graben, North Sea. In M. Halbouty, Giant oil and gas fields of the decade 1968-1978, AAPG Memoir 30, 59-80.

Hu, S., Zhao, W., Xu, Z., Zeng, H., Fu, Q., Jiang, L., Shi, S., Wang, Z., & Liu, W. (2017). Applying principal component analysis to seismic attributes for interpretation of evaporite facies: Lower Triassic jialingjiang formation, Sichuan Basin, China. Interpretation, 5(4), 461–475. https://doi.org/10.1190/int-2017-0004.1

Johnson, S., & Watt, J. (2012). Influence of fault trend, bends, and convergence on shallow structure and geomorphology of the Hosgri strike-slip fault, offshore central California. Geosphere, 8. https://doi.org/10.1130/GES00830.1

Luo, Y., Al-Dossary, S., Marhoon, M., & Alfaraj, M. (2003). Generalized Hilbert transform and its application in geophysics. The Leading Edge, 22, 198–202.

Martini, M., & Ortega-Gutiérrez, F. (2018). Tectono-stratigraphic evolution of eastern Mexico during the break-up of Pangea: A review. Earth-Science Reviews, 183, 38–55. https://doi.org/10.1016/j.earscirev.2016.06.013

Meckel, T. A., & Mulcahy, F. J. (2016). Use of novel high-resolution 3D marine seismic technology to evaluate quaternary fluvial valley development and geologic controls on shallow gas distribution, inner shelf, Gulf of Mexico. Interpretation, 4(1), 35–49. https://doi.org/10.1190/int-2015-0092.1

Mitchum, R. M., Van Wagoner, J. C., Taylor, G., & Dockery, D. T. (1990). High-frequency sequences and eustatic cycles in the Gulf of Mexico Basin. Sequence Stratigraphy as an Exploration Tool: Concepts and Practices in the Gulf Coast, 11th Annual, 257–267. https://doi.org/10.5724/gcs.90.11.0257

Mitchum, R. M., Vail, P. R., & Thompson, S. (1977). Seismic stratigraphy and global changes of sea level, part 2the depositional sequence as a basic unit for stratigraphic analysis1. Seismic Stratigraphy — Applications to Hydrocarbon Exploration, 53–62. https://doi.org/10.1306/m26490c4

Peltier, W. R. (2005). On the hemispheric origins of meltwater pulse 1a. Quaternary Science Reviews, 24, 1655–1671. https://doi.org/10.1016/j.quascirev.2004.06.023

Pigott, J., Zhai, R., Pigott, K., & Tonianse, T. (2011). Searching for the missing link: The regressive system tract - seismic stratigraphic evidence from the southern Gulf of Thailand. All Days, 1–24. https://doi.org/10.2523/iptc-15113-ms

Posamentier, H. (2001). Lowstand alluvial bypass systems: Incised vs. unincised. AAPG Bulletin, 85(10), 1771-1793.

Radovich, B. J., & Oliveros, R. B. (1998). 3D sequence interpretation of seismic instantaneous attributes from the Gorgon Field. The Leading Edge, 17, 1286–1293.

Reijenstein, H. M., Posamentier, H. W., & Bhattacharya, J. P. (2011). Seismic Geomorphology and high-resolution seismic stratigraphy of inner-shelf fluvial, estuarine, Deltaic, and marine sequences, Gulf of Thailand. AAPG Bulletin, 95(11), 1959–1990. https://doi.org/10.1306/03151110134

Roberts, A. (2001). Curvature attributes and their application to 3D interpreted horizons. First Break, 19, 85-99.

Saha, A., & Bhattacharya, B. (2023). Controls of allogenic factors on the development of fluvial sequence stratigraphic architecture: A case study. Journal of Earth System Science, 132(1), 1–17. https://doi.org/10.1007/s12040-022-02038-1

Scamardo, E., & Kim, W. (2016). How Do River Meanders Change with Sea Level Rise and Fall? American Geophysical Union, Fall Meeting 2016, Abstract #EP53G-08. https://doi.org/2016AGUFMEP53G..08S

Simms, A., Anderson, K., Taha, Z., & Wellner, J. (2007). Geomorphology and the age of the oxygen isotope stage 2 (last lowstand) sequence boundary on the northwestern Gulf of Mexico continental shelf. Geological Society of London, 29–46.

Souza, R., Lumley, D., Shragge, J., Davólio, A., & Schiozer, D. J. (2019). 4D seismic bandwidth and resolution analysis for reservoir fluid flow model applications. ASEG Extended Abstracts. https://doi.org/10.1080/22020586.2019.12073147

Taner, M. T., Koehler, F., & Sheriff, R. E. (1979). Complex seismic trace analysis. Geophysics, 44, 1041–1063.

Van Wagoner, J. C. (1995). Overview of Sequence Stratigraphy of Foreland Basin Deposits: Terminology, Summary of Papers, and Glossary of Sequence Stratigraphy. In J. C. Van Wagoner & G. T. Bertram, Sequence Stratigraphy of Foreland Basin Deposits: Outcrop and Subsurface Examples from the Cretaceous of North America. AAPG, vol. 64, 9–21.

Van Wagoner, J. C., Mitchum, R. M., Campion, K. M., & Rahmanian, V. D. (1990). Siliciclastic sequence stratigraphy in well logs, cores, and outcrops. AAPG Methods in Exploration, 1–55. https://doi.org/10.1306/mth7510

Vail, P., Todd, R., & Sangree, B. (1977). Seismic stratigraphy and Global Changes of Sea Level: Part 5. Chronostratigraphic Significance of Seismic Reflections: Section 2. Application of Seismic Reflection Configuration to Stratigraphic Interpretation. Memoir 26, 99–116.

Vail, P. R., Mitchum Jr., R. M., & Thompson III, S. (1977). Seismic stratigraphy and global changes of sea level, part 4: global cycles of relative changes of sea level. In C. E. Payton, Seismic Stratigraphy—Applications to Hydrocarbon Exploration. AAPG, Memoir 26, 83-97.

Waelbroeck, C., Labeyrie, L., Michel, E., Duplessy, J. C., McManus, J. F., Lambeck, K., Balbon, E., & Labracherie, M. (2002). Sea-level and deep water temperature changes derived from benthic foraminifera isotopic records. Quaternary Science Reviews, 21, 295–305. https://doi.org/10.1016/S0277-3791(01)00101-9

Weimer, R. (1992). Presidential Address: Developments in sequence stratigraphy: Foreland and Cratonic Basins. AAPG Bulletin, 76, 965–982. https://doi.org/10.1306/bdff893e-1718-11d7-8645000102c1865d

Wright, J. D. (2000). Global climate change in marine stable isotope records. In Noller, J. S., Sowers, J. M., & Lettis, W. R., *Quaternary geochronology: Methods and applications*, American Geophysical Union, 427–433.

Wurbs, R., & Zhang, Y. (2016). Analyses of Flows of the Brazos and Trinity Rivers and Tributaries. Texas Water Development Board. https://www.twdb.texas.gov/publications/reports/contracted_reports/doc/1348311643_TAMU.pdf

Xie, F., Wu, Q., Wang, L., Shi, Z., Zhang, C., Liu, B., Wang, C., Shu, Z., & He, D. (2017). Passive continental margin basins and the controls on the formation of evaporites: a case study of the Gulf of Mexico Basin. Carbonates and Evaporites, 34(2), 405–418. https://doi.org/10.1007/s13146-017-0404-z

Yao, Q., Joshi, S., Liu, K., Yao, Q., & Yin, D. (2022). A multi-decadal analysis of river discharge and suspended sediment load in three Texas coastal rivers in relation to hurricanes, seasonal rainfall, and ENSO. Frontiers in Earth Science, 10.

Zhao, T., Jayaram, V., Roy, A., & Marfurt, K. J. (2015). A comparison of classification techniques for seismic facies recognition. Interpretation, 3, SAE29-SAE58.

APPENDICES

Appendix A. Frequency distribution through the interval of interest—0 to 200 milliseconds.

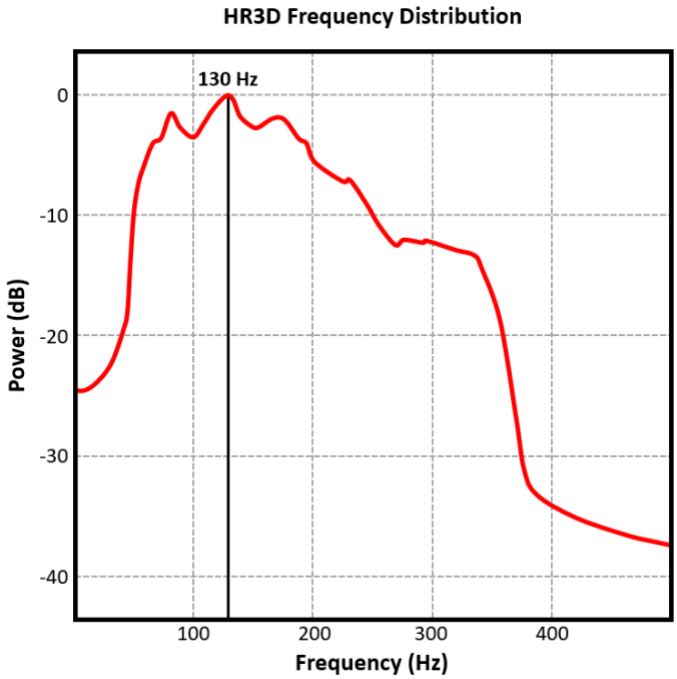

Appendix B. Peak frequency extracted along each unconformity.

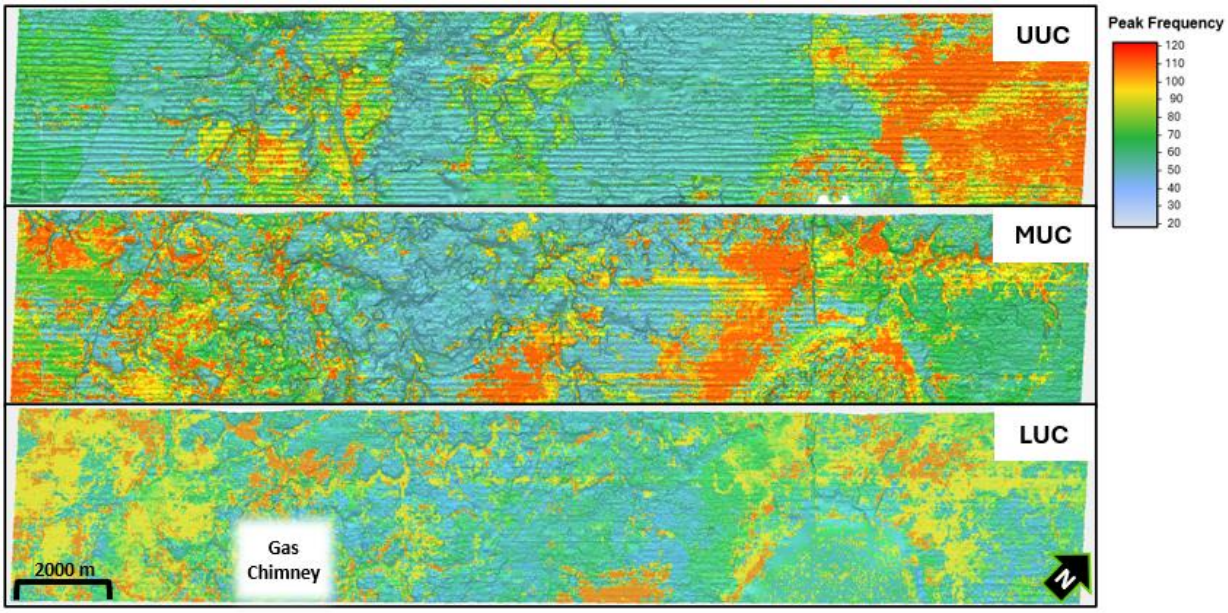

Appendix C. Peak magnitude extracted along each unconformity.

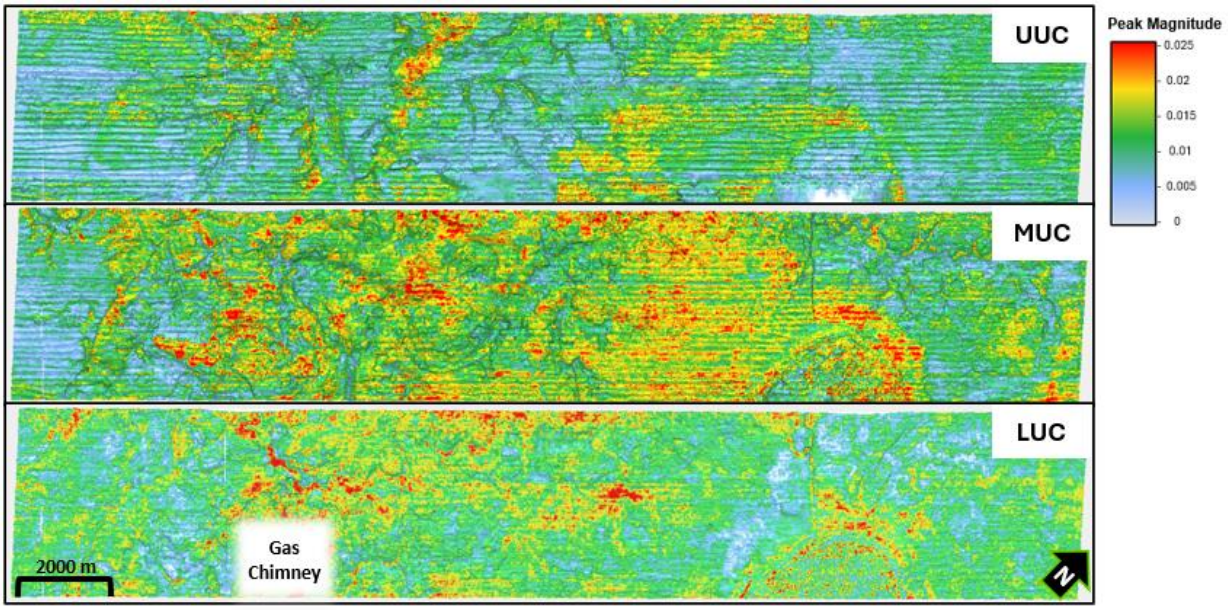

Appendix D. Spectrally balanced amplitude extracted along the maximum flooding surfaces (MFS) of each depositional sequence.



Appendix E. Sweetness extracted along the maximum flooding surfaces (MFS) of each depositional sequence.

